International Journal of Solids and Structures 51 (2014) 1901–1922

Contents lists available at ScienceDirect

International Journal of Solids and Structures

journal homepage: www.elsevier.com/locate/ijsolstr

Thermomechanical modelling of a NiTi SMA sample submitted to displacement-controlled tensile test

Dorian Depriester [1], Anne Maynadier *, Karine Lavernhe-Taillard, Olivier Hubert

LMT-Cachan, ENS Cachan, CNRS UMR 8535, Univ. Paris 6, PRES UniverSud Paris, 61 Avenue du Président Wilson, F-94235 Cachan Cedex, France

ARTICLE INFO

Article history:
Received 25 July 2012
Received in revised form 14 November 2013
Available online 19 February 2014

Keywords:
Shape Memory Alloys
Nitinol
Martensitic phase transformation
Thermomechanical coupling
Transformation bands

ABSTRACT

Shape Memory Alloys (SMAs) undergo an austenite–martensite solid–solid phase transformation which confers its pseudo-elastic and shape memory behaviours. Phase transformation can be induced either by stress or temperature changes. That indicates a strong thermo-mechanical coupling. Tensile test is one of the most popular mechanical test, allowing an easy observation of this coupling: transformation bands appear and enlarge giving rise to a large amount of heat and strain localisation. We demonstrate that the number of transformation bands is strongly associated with the strain rate. Recent progress in full field measurement techniques have provided accurate observations and consequently a better understanding of strain and heat generation and diffusion in SMAs. These experiments bring us to suggest the creation of a new one-dimensional thermomechanical modelling of the pseudo-elastic behaviour. It is used to simulate the heat rise, strain localisation and thermal evolution of the NiTi SMA sample submitted to tensile loading.

1. Introduction

Since their discovery in the early 60's, Shape Memory Alloys (SMAs) have been widely studied leading to a great improvement in the understanding of their behaviour (pseudo-elasticity and shape memory effect), (Bhattacharya, 2003; Lagoudas et al., 2006; Patoor et al., 2006; Shaw and Kyriakides, 1995). The progress made promoted their use in many applications, especially in the medical field for bio-compatible NiTi-based SMAs (Chevalier et al., 2010). A generalisation of SMAs' use for structures with increasing complexity requires the development of more efficient models, reflecting the overall behaviour but also taking into account the strong thermo-mechanical coupling and its effects (strain localisation, heat emission and thermal phenomena).

Indeed, whilst submitted to a simple displacement-controlled tensile test, pseudo-elasticity occurs in SMAs. Pseudo-elasticity corresponds to the ability of the material to elongate in large proportion (up to 8%) under tensile loading and to recover to its prior shape when unloaded. Pseudo-elasticity is caused by a phase transformation between the austenitic (A) and martensitic (M) phases (Bhattacharya, 2003). The phase transformation leads to a distortion of the crystal lattice, that causes the increase of strain. Associated with low strengthening, localisation usually occurs leading to so-called "transformation bands".

The phase transition is associated with heat emission (or absorption during a reverse loading). Since the phase transformation is induced either by temperature or stress, the local temperature fluctuations strongly change the rate of transformation bands. He and Sun (2010) or Shaw and Kyriakides (1995) for instance have investigated the dependence of the localisation phenomenon on the loading rate. As the transformation can be induced by temperature changes, the behaviour is highly dependent on the competition of the two transient thermal phenomena: how fast the latent heat is released (i.e. loading rate) and how fast it is evacuated (by conduction and air convection). Indeed, if natural evacuation is too weak to compensate the released heat at the front of the band, the transformation is hampered. Thus a new localisation band borns, where the transformation is easier, at the lowest temperature-point of the sample (stress considered as homogeneous) (Shaw and Kyriakides, 1997). Therefore, the number of bands is well linked to the thermal conditions and the loading rate. The following experimental law, established by Zhang et al. (2010), associates the strain rate ($\dot{\varepsilon}$) with the maximum number of localised bands, denoted n_{max}:

* Corresponding author. Present address: Laboratoire de Mécanique des Contacts et des Structures (LaMCoS) Université de Lyon/ INSA-Lyon/ UMR CNRS 5259, 20 Avenue Albert Einstein, 69621 Villeurbanne, France. Tel.: +33 04 72 43 82 72; fax: +33 04 72 43 89 13.

E-mail address: anne.maynadier@insa-lyon.fr (A. Maynadier).

[1] Present address: MINES ParisTech – Centre de Mise en Forme des Matériaux, BP 207, F-06904 Sophia-Antipolis, France.

http://dx.doi.org/10.1016/j.ijsolstr.2014.01.027
0020-7683/

$$n_{max} = C\dot{\varepsilon}^m \quad (1)$$

where C is a constant, depending on the boundary conditions, conductivity and heat convection. It is shown that m is between 0.5 and 1 (He and Sun, 2010).

On the other hand, recent progress in imaging techniques has allowed an improvement in the quality of the observations. For instance, He and Sun (2010) and Feng and Sun (2006) used oblique light and cameras to evidence the transformation bands. Full field measurement such as Digital Image Correlation (DIC) and InfraRed Thermography (IRT) are particularly well suited for the observation of this phenomenon. Indeed they provide quantitative information (displacement or temperature) at each point on the surface. It opens a field for the study of coupled phenomena -for instance the main idea is to use these quantities to infer the heat sources associated to phase transformation (Schlosser et al., 2007; Chrysochoos, 2002).

There are numerous articles of literature available on this topic (Schlosser et al., 2007; Delpueyo et al., 2012) even related to dynamic conditions (Nemat-Nasser et al., 2005). The authors of the present paper have proposed a new correlation method in order to extract thermal and kinematic quantities from a single set of infrared images and a single computation (Maynadier et al., 2012). This technique is described in the first part of this article (Section 2). Once applied to a tensile strained NiTi SMA, the main phenomena described above are highlighted. A quantitative evaluation of transformation strain and of thermal gradient at the front of the bands is made. The second part of this paper (Section 3) is introducing a one-dimensional model of a sample submitted to a displacement-controlled tensile test based on the Clausius–Clapeyron diagram (Stress vs. Temperature). The computing thermal scheme is first presented, then each phenomenon is introduced gradually in order to obtain a fully coupled model able to describe homogeneous transformation as well as localisation, unloading and cycling. The corresponding algorithm and numerical methods are briefly stated in the third part (Section 4). The fourth part (Section 5) proposes a qualitative validation of the one-dimensional model, run with a set of parameters supported by existing literature, against several loads. Numerical results are compared from the experiments conducted at different strain rates. The square-root link between loading rate and number of bands stated by Zhang et al. (2010) and analytically modelled by He and Sun (2010) is verified. The ultimate part discusses the ability of the one-dimensional thermomechanical model to simulate more complex situations. To conclude, improvements are suggested.

2. Observation of martensitic transformation bands as a result of full-field measurements

This section aims at introducing the three key points of the NiTi SMA behaviour under tensile loading which are:

- uniform transformation,
- localisation in narrow bands of transformation and enlargement,
- relationship between number of bands, velocity of front band and loading conditions.

Full field measurement techniques are particularly well indicated for observations and measurement of heterogeneous mechanical and thermal quantities. Indeed transformation bands involves local displacement and localised heat emissions. Many research groups used DIC to obtain kinematic fields and IRT to obtain thermal fields (Delpueyo et al., 2012; Favier et al., 2007; Pieczyska et al., 2006). The InfraRed Image Correlation (IRIC) is a recent global correlation method: correlation is applied on a single set of infrared images, that delivers in one calculation both thermal and kinematic measurements at each point of a single Finite Element Mesh over the zone of interest (ZOI). The determination of both quantities is done jointly in a fully coupled manner. It has three advantages: simplifying the experimental set up (only one IR camera), avoiding the time and space pairing of the two fields, and not requiring expensive optical filters nor separator cubes. For more details on the IRIC technique employed hereafter the reader could refer to Maynadier et al. (2012).

2.1. Experimental set up

The material used for the test is a $Ni_{49.75at\%}Ti$ alloy (commercial name *SE*508) produced by Nitinol Devices and Components (Fremont, California, USA). Samples are formed by Nitifrance (Lury-sur-Arnon, France). The forming process consists mainly in a cold-rolling and subsequent 2 min heat treatment at 480°C in a salt bath. Samples are flat bone shaped. Their cutting was performed by electro-erosion machining. The surface was electro-chemically polished. The S_0 section is rectangular (20×2 mm^2) and the gauge length L_0 is 120 mm long.

The forming process provides polycrystalline specimen with a mean grain size of about 30μm. At room temperature, the material is fully Austenitic (face-centered cubic symmetry).

Differential Scanning Calorimetry (DSC) measurements have been performed (Maynadier et al., 2012) using a 50 mg sample and a Heat/Cool/Heat method (heating rate: 10 K min^{-1}; cooling rate -3 K min^{-1}). Results are reported in Fig. 1. This curve exhibits two transitions during cooling corresponding to the transition limits between *A* phase and *R* (rhombohedral symmetry) phase then between *R* phase and *M* (monoclinic symmetry) phase. We estimate the following transitions: Austenite start $A_s = 15$°C, Austenite finish $A_f = 40$°C, martensite start $M_s = -10$°C and martensite finish $M_f = -30$°C. The *R*-phase does occur and may be present at room temperature during our experiments. It will not be considered in the modelling since the deformation associated to is much lower than that associated with *A* to *M* phase transition. Moreover a controversy does exist about the appearance of *R* phase during a tensile test at room temperature.[2] The DSC measurement allows us to estimate latent heats of phase transformations. The latent heat corresponding to *R* to *M* phase transformation (red area in the figure) will be retained for the modelling $\Delta H_{R-M} \approx 9$ Jg^{-1}.[3]

The tensile tests were performed on a 100 kN hydraulic MTS machine. The sample was installed in the hydraulic jaws. The experimental workspace, including imaging devices, was protected in order to keep the thermal and ventilation conditions as constant as possible. During the tests, the ambient temperature of the workspace was 28 ± 0.5°C. Many displacement rates $\dot{\delta}$ have been explored from 0.002 mm s^{-1} to 0.02 mm s^{-1}. The tests reported below have been conducted using $\dot{\delta} = 0.01$ mm s^{-1} and 0.05 mm s^{-1} corresponding to strain rates $\dot{\delta}/L_0 = 8.3x10^{-5}$ s^{-1} and $4.2x10^{-4}$ s^{-1} respectively.

The displacement and thermal full field measurement were performed thanks to InfraRed Image Correlation. For this technique, an infrared camera and a large black body at low temperature are required. We used a Cedip Jade III infrared camera recording at 100 Hz with an Integration Time (IT) of 930 µs. This particular IT was chosen to cover a temperature range up to 60 °C. Indeed we are operating at 28°C and, in the considered loading rate, the

[2] Even if *R* phase appears first during cooling denoting a lower chemical energy density than *M* phase, elastic energy density associated to *R* phase is much lower, that could make the *M* phase more stable during tensile strengthening.

[3] Latent heat associated with *M* to *A* transition is much higher ($\Delta H_{M-A} \approx 25$ Jg^{-1}) and leads to high temperature variations that have not been observed experimentally. Both *R* and *A* phases are probably present in the material at its initial state.

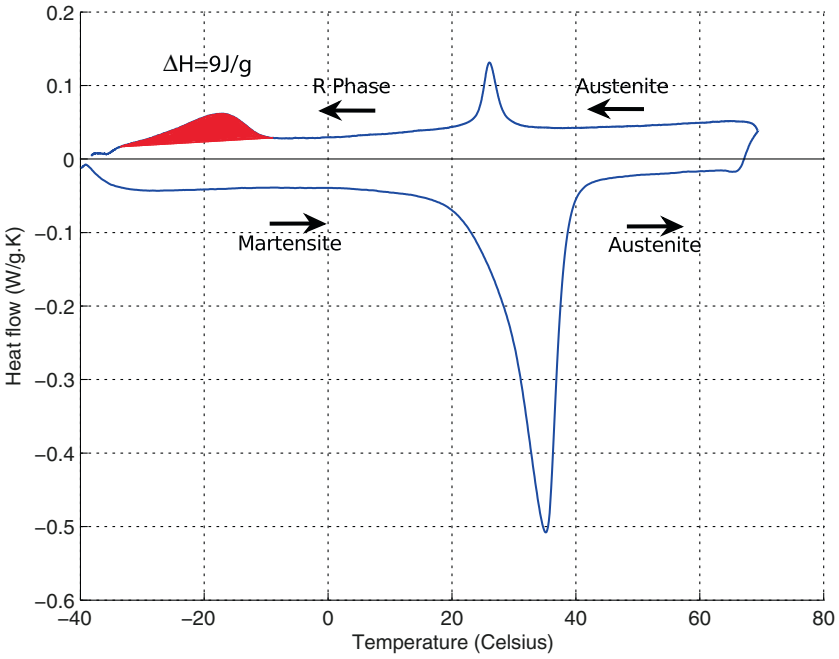

Fig. 1. Differential scanning calorimetry of a $Ni_{49.75}$ at % *Ti*.

temperature of our structure can rise to 30 °C. The devices are set up as shown in Fig. 2(a). The gauge surface is covered with a speckle pattern of high emissivity black paint (0.95) over the polished surface of the sample exhibiting a low emissivity (around 0.2). Consequently the black dots have an emission which is directly related to the temperature of the surface whereas the radiation coming from the nude surface areas is a mixture between the temperature of the sample itself and the temperature of the reflecting cold black body. Thus, on the one hand the speckle visible in the IR pictures from the grey level recorded (see Fig. 2(b)) allows us to calculate the displacement field by image correlation. On the other hand, the temperature of surface can be inferred at each point, knowing the black body temperature. More details are available in Maynadier et al. (2012), especially the calibration steps required to obtain quantitative and reliable measurements. The performances of the correlation code were estimated. It reveals that the uncertainties are dependent on the mesh size, as for any other correlation code. However, the displacement mean error and uncertainty (due to the calculation) are lower than 0.05 pixels for a 12×12 pixels mesh size; the strain uncertainty is around 5×10^{-4}; the thermal uncertainty oscillates between 10^{-3}°C and 10^{-4}°C (this numerical uncertainty is lower than the Noise Equivalent Thermal Deviation of the camera).

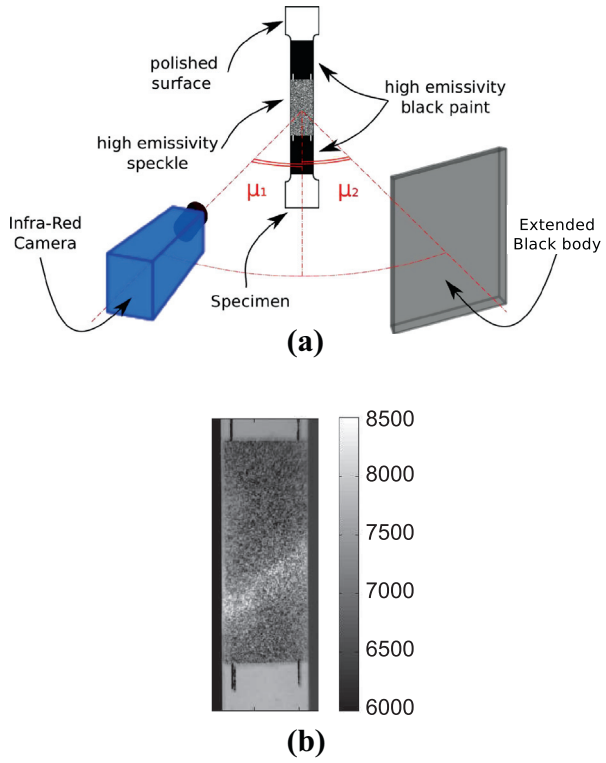

Fig. 2. (a) Experimental set-up showing the relative position of IR camera, specimen surface and extended black body. (b) Infra-red raw picture observed during tensile test on Ni-Ti SMA showing the speckled specimen face undergoing a strain and heating localisation. The measurement ranges between 0 and 16000 digital levels (DL). The colorbar indicates the grey intensity whose variation could be interpreted as temperature changes thanks to an appropriate calibration. (Maynadier et al., 2012).

2.2. Tensile test

The curves plotted in Fig. 3(a) give the engineering stress–strain (*i.e.* F/S_0 *vs.* δ/L_0 with F the axial force) behaviour of the material for the two different strain rates. The shape is typical of pseudo-elasticity[4]: a first linear part -step I- (ended around 350 MPa and 1.1%) usually interpreted as elasticity of the *A* phase (even if *A* to *R* phase may partially occur); an inflection point followed by a strain plateau of 4.6% of magnitude -step II- corresponding to the localisation step and appearance of *M* phase; and a final strengthening -step III- usually associated to a transition from phase transformation to elastic behaviour of *M* phase (only perceptible for lowest strain rate

[4] Pseudo-elasticity strongly depends on room temperature. At low temperature martensite reorientation occurs leading to so-called memory effect; at high temperature *A* to *M* phase transformation occurs leading to pseudo-elasticity. In the present case and in agreement with DSC measurements, *M* to *A* transformation occurs at room temperature so that the reverse transformation during unloading may be partial as observed in Fig. 3(a).

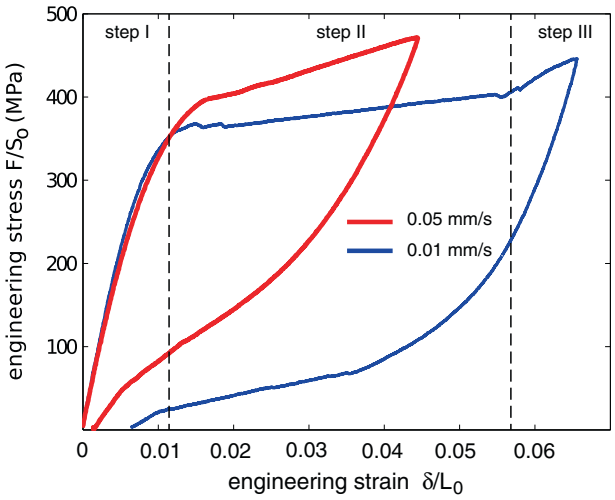

(a)

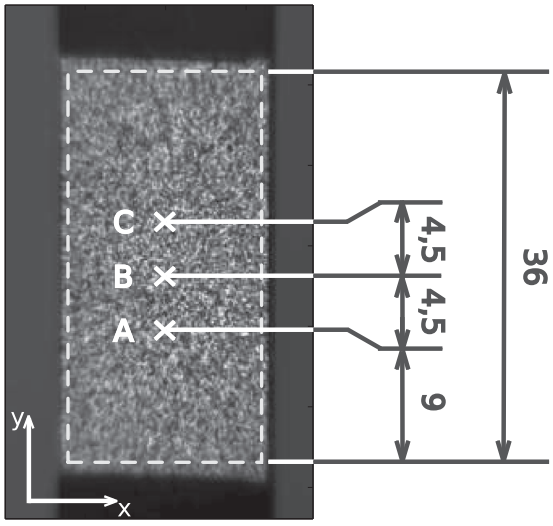

(b)

Fig. 3. (a)- Experimental tensile curves at $\dot{\delta}/L_0 = 8.3 \times 10^{-5}$ s^{-1} and 4.2×10^{-4} s^{-1}, (engineering stress *vs.* strain). (b)- Raw image of the sample before tensile testing. The area of interest is embodied by the dotted lines. *A*, *B* and *C* are some physical points where thermomechanical quantities are highlighted (Lagrangian description). Dimensions are given in mm.

test). Higher strain rate leads to a higher slope of plateau and a global higher stress level. We will see in the next subsections that the phenomena are not so clearly partitioned. The engineering stress and strain are calculated from macroscopic quantities given by the sensors of the testing machine (force F and displacement δ). Although stress–strain curve is corrected taking into account the rigidity of machine and grip, the behaviour is flawed since the heterogeneous character of the deformation is not accessible. Thus the investigation of the thermal and kinematic fields and their confrontation to the tensile curve will generate a valuable amount of information.

The results plotted in Fig. 4 justify, by itself, the use of full field measurements. The figure shows the simultaneity of longitudinal strain $\varepsilon = \varepsilon_{yy}$ and temperature rise at the three different physical points on the surface previously defined (see Figs. 3 and 5) compared to the macroscopic quantities: strain and temperature are first uniform (step I), then non uniform (step II) denoting the birth of a transformation band at the 44th second of the highest strain rate test ($\dot{\delta}/L_0 = 4.2 \times 10^{-4}$ s^{-1}). The strain at point A increases up to 6% and saturates. The band enlarges and the heat is released only at the front of the band. The full field measurements in Fig. 5 confirm this interpretation. A systematic simultaneity of strain increase and heat release is observed. Before localisation, a diffused appearance of martensite is highlighted. The linear stress–strain macroscopic behaviour is consequently a mix between diffuse transformation strain and elastic behaviour of the (A) phase. After localisation, heat diffusion is clearly highlighted since the thermal band is wider than the strain band. The local character of the measurements, coupled with the high temporal discretisation allows an accurate observation of the birth and propagation of the bands. These points are more deeply discussed in the next paragraphs.

2.3. Uniform transformation step (I)

As shown in Fig. 4, the first step (I) does not only correspond to an elastic behaviour. Indeed, the thermoelasticity should induce a cooling of the surface in the very first moments of the tensile test. On the contrary, we observe after 2 or 3 s that the temperature increases uniformly over the surface. At the same time, the longitudinal strain increases uniformly. We can therefore conclude that a diffuse phase transformation occurs. It convinces us that thermoelasticity is probably negligible for this test (low strain rate leading to low stress rate).

2.4. Localisation step (II)

During the uniform step (I), strain is perfectly uniform, whereas the thermal field exhibits a smooth gradient (less than 0.3°C at room temperature and less than 0.6°C over 700 mm^2 at 33°C) due to heat diffusion and convection. The transformation localises at the 44th second: the strain stops increasing uniformly and some points on the surface undergo sudden strain and temperature rise. One may notice that the localisation first occurs close to the heads of the specimen due to the additional multi-axial loading and cooler temperature in the clamps. This area is out of the view field thus the observed bands in Fig. 5 are not the very first ones. Localisation results in a simultaneous rise of temperature and strain along a line oriented of 55° from the tensile direction. Inside the band, the strain rises until it saturates at 0.06 and the temperature locally increases by more than 10°C (depending on the ventilation of the workspace and the loading rate). On the other hand, the heat emitted during the appearance of the band goes against the transformation. So if the diffusion or convection is not fast enough compared to the strain rate, the transformation stops in the band, and another appears where stress and temperature conditions are more favourable. Otherwise the transformation spreads to the front of the band, and it begins to widen. These phenomena occur during the plateau of the engineering curve (step II). Sometimes, a small drop in stress can be observed due to the relaxation induced by the localisation (here the plateau is not a straight line, see also Shaw and Kyriakides, 1995). Thus, out of the bands (point C), strain tends to decrease slightly.

These results provide us with some useful informations for the modelling of the tensile test: we can first assume that strain rate and heat rate are coupled via the volume ratio of the transformed phase; secondly $\varepsilon_{sat} = 0.06$ is the maximal longitudinal strain that can be reached in one physical point; we will finally consider that only the A to M and/or M to A transformations can occur during the tensile test, neglecting the role of R phase not perceptible on experimental results (except for DSC).

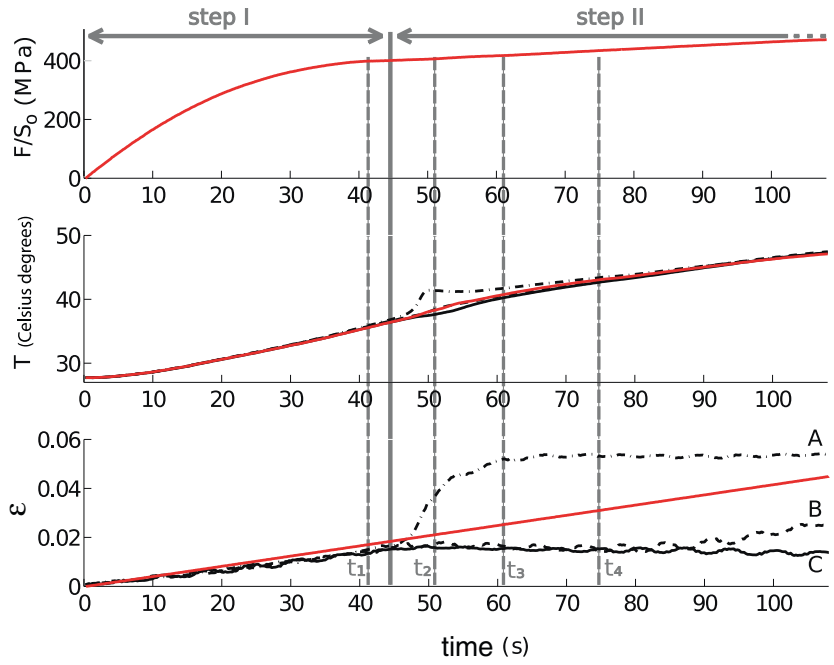

Fig. 4. Simultaneous evolution of stress, temperature and longitudinal strain. Red lines are macroscopic quantities whereas doted lines are local quantities at the three physical points (A,B,C) – at $\dot{\delta}/L_0 = 4.2 \times 10^{-4}\ s^{-1}$. (For interpretation of the references to color in this figure legend, the reader is referred to the web version of this article.)

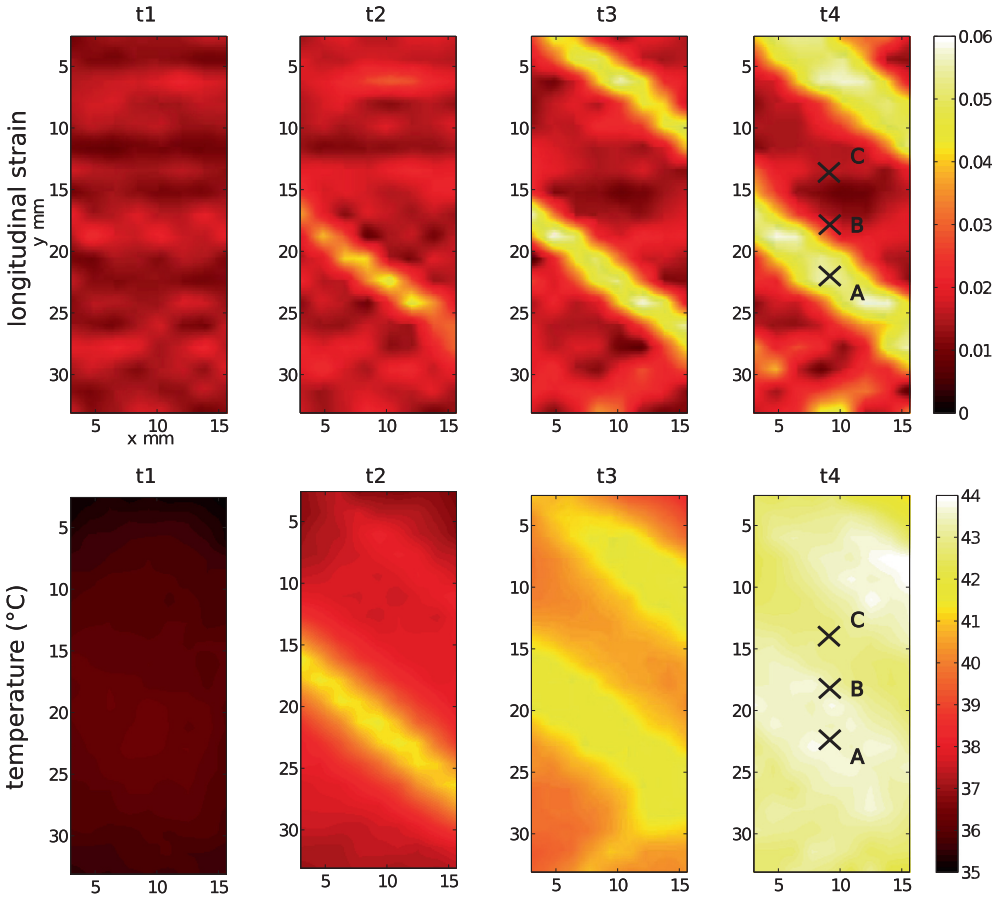

Fig. 5. Temperature and longitudinal strain fields at four typical instants ($t_1 = 42$ sec, $t_2 = 51.25$ sec, $t_3 = 61.25$ sec, $t_4 = 75$ sec) – at $\dot{\delta}/L_0 = 4.2 \times 10^{-4}\ s^{-1}$.

3. Modelling

Many remarkable works have been done in order to model the specific behaviour of SMAs. However in most cases, only one aspect of the behaviour is described over others. Among these works, Hu et al. (2006) use a kinematic criterion, neglecting the homogeneous stage to calculate the width of the localised band. This model assumes that only one band occurs in the middle of the sample. On the contrary, some studies (De la Flor et al., 2006; Auricchio et al., 1997) are based on the Clausius–Clapeyron diagram in order to deduce the martensitic ratio from the stress. Those ones are able to take the elastic strain and temperature into account. Nevertheless the Clausius–Clapeyron diagram is only valid on the homogeneous stage, so those models can not reproduce the localisation phenomenon. Some energetic approaches (Thamburaja and Nikabdullah, 2009; Christ and Reese, 2009; Levitas and Stein, 1997) can be used to model the transformation dealing with the free energy associated to the phase transformation. These approaches are usually applied to get the homogeneous behaviour of a representative volume element. It should be associated to Finite Element Modelling (FEM) in order to model the localisation. Another modelling strategy is applied in Shaw (2000): it is based on a benchmark which presents isothermal macroscopic tensile curves at different temperatures. Each curve is interpolated and implemented in a FEM solver. Then, this software is able to model the transformation strain (considered as a plastic-like flow) and calculate the heat associated to this flow. Considering the local temperature at each point, the adequate tensile curve is used. This method gives good results concerning the tensile curve, but it can not simulate the local behaviour (no distinction between the two stages *i.e.* homogeneous and heterogeneous) and unloading (reverse M to A transformation). Finally, attention must be paid to the very complete work of Chang et al. (2006) after Shaw (2002) which proposes a model based on a 1D Helmholtz free energy with strain gradient effects and phase fractions as internal variables. In this approach, softening associated to phase transformation can lead to localisation and propagation in the strain, phase fraction, and temperature fields. In this work the homogeneous stage is nevertheless neglected.

So, it has been figured out that no model is able to simulate all of the following aspects for a tensile test specimen as presented in the previous experimental section:

1. (a) homogeneous transformation stage,
   (b) heterogeneous transformation stage,
2. temperature dependence of the localisation phenomenon,
3. exo/endo -thermic reactions,
4. reversibility (mechanical) transformations (loading/unloading).

In the approach proposed herewith, we choose to model the behaviour of the sample as a one-dimension problem. That means that the considered thermo-mechanical variables are only dependent on time t and axial position x. It implies that the angle of the localisation bands cannot be represented.

Fig. 6 brings the notations used. The initial gauge length of sample is denoted L_0. Initial cross section and outer length are denoted respectively S_0 and ℓ. The specimen is clamped in grips at each extremity, that act as mass of high thermal inertia at constant temperature T_{clamp}. The gauge zone is surrounded by unventilated air assumed at constant temperature T_{air}. Consequently, thermal boundary conditions are convection with air on the free surface of the sample (power loss $\dot{q}_{dis}$) and conduction ensured by clamps.

The internal variables of the model are defined as a function of x and t (axial and temporal index): we use $f(x,t)$ the Martensitic ratio, defined between 0 and 1, $T(x,t)$ the temperature, $\sigma(t)$ the axial stress considered as position-independent (homogeneous stress due to quasi-static phenomena).

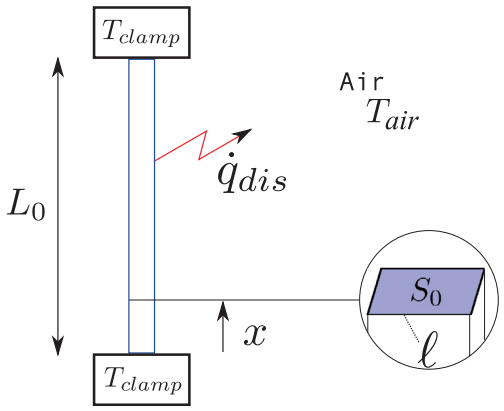

Fig. 6. One-dimensional model.

3.1. Thermal equations

Thanks to 1D problem assumptions, temperature gradients in both transverse directions are neglected *i.e.* temperature is homogeneous over the section S_0. Let define $\dot{q}_{tr}$ and $\dot{q}_{th}$ the transformation and the thermoelastic power in a current cross section at position x and time t. They are considered as source in the heat equation:

$$\dot{q}_{tr} = \rho \dot{f}(x,t)\Delta H \tag{2a}$$

$$\dot{q}_{th} = -\alpha(x,t)T(x,t)\dot{\sigma}(t) \tag{2b}$$

ΔH denotes the latent transformation heat from A to M, $\rho(x,t)$ the local density and $\alpha(x,t)$ the local thermal expansion factor. Since the problem is one-dimensional, we can consider the air convection of the sample as a volumetric power loss:

$$\dot{q}_{dis} = \frac{dP_{conv}}{dV} = \frac{h\ell}{S_0}(T(x,t) - T_{air}) \tag{3}$$

h being the convection factor and T_{air} the temperature of air. Finally, the heat equation gives:

$$\lambda \Delta T + \rho \dot{f} \Delta H - \alpha T \dot{\sigma} - \frac{h\ell}{S_0}(T - T_{air}) = \rho C_p \frac{\partial T}{\partial t} \tag{4}$$

with $\lambda(x,t)$ the thermal conductivity and C_p the thermal capacity. The boundary conditions can be defined as:

$$-\lambda(0,t)\left.\frac{\partial T}{\partial x}\right|_0 = h_c\left(T_{clamp} - T(0,t)\right) \tag{5a}$$

$$-\lambda(L_0,t)\left.\frac{\partial T}{\partial x}\right|_{L_0} = h_c\left(T(L_0,t) - T_{clamp}\right) \tag{5b}$$

where h_c is the conductance factor between the sample and the clamps. In the following, we consider $T_{clamp} = T_{air}$ as true all along the test.

3.2. Phase transformation flow rule

As proposed in Auricchio et al. (1997) and initially by Koistinen and Marburger (1959) for its integrated exponential form, the volume fraction of martensite $f(x,t)$ is supposed to obey to a first order flow rule:

$$\dot{f}(x,t) = \frac{\partial f}{\partial t} = V_t(f_t(x,t) - f(x,t)) \tag{6}$$

where $f_t(x,t)$ is the phase transformation driving force (or martensite ratio "at equilibrium") and V_t is the maximum transformation rate. The differential equation permits a delay between the driving force $f_t(x,t)$ and the martensitic ratio $\dot{f}(x,t)$ evolution. It models the non-instantaneous effect of phase transformation in accordance with the temporal evolution of the strain in a physical point where the localisation band nucleates (see Section 2). It must be noticed that this simple flow rule is not able to reproduce the complexity of real phase transformation, meaning that only A and M phases are considered. This formulation ensures us on the other hand to verify the second principle (positive dissipation) since the thermodynamic force Y associated to internal variable $\dot{f}$ satisfies (Shaw, 2002; Chang et al., 2006):

$$\Delta H = Y - T\frac{\partial Y}{\partial T} \quad \text{and} \quad Y\dot{f} \geqslant 0 \tag{7}$$

This simplicity allows us finally to put forward a robust finite difference modelling able to give back the complexity of birth and propagation of localisation bands.[5]

3.3. Mechanical equations

We use a classical partition of the strain in elastic strain ε_{el}, thermal strain ε_{th}, and transformation strain ε_{tr}, giving for a one-dimensional problem:

$$\varepsilon(x,t) = \varepsilon_{el}(x,t) + \varepsilon_{th}(x,t) + \varepsilon_{tr}(x,t) \tag{8}$$

Thermoelasticity has not been considered in the modelling in accordance with experimental results. The elastic strain obeys to Hooke's law: $\varepsilon_{el}(x,t) = \frac{\sigma(t)}{E(x,t)}$ with E the Young modulus. The definition of the transformation strain at point x cannot be done without evaluating the question of spatial resolution of the modelling tool. At the variant scale, ε_{tr} gets two possible values: zero if the matter remains austenitic or ε_{sat} the maximum transformation strain if the matter becomes martensitic. This binary solution is not acceptable for the continuum modelling we want to build. The suggested model is macroscopic so that we have to consider that physical point x is corresponding to a volume involving a large number of grains, large enough so that the transformation strain can be defined aslinearly dependent of the martensite volume fraction:

$$\varepsilon_{tr}(x,t) = f(x,t)\varepsilon_{sat} \tag{9}$$

This expression implies that the modelling is a serial 1D modelling (homogeneous stress approximation). Thermal strain is defined by:

$$\varepsilon_{th}(x,t) = \alpha(T(x,t) - T_{air}) \tag{10}$$

where α is the current thermal expansion factor. The definition of total strain becomes:

$$\varepsilon(x,t) = \frac{\sigma(t)}{E(x,t)} + \alpha(T(x,t) - T_{air}) + f(x,t)\varepsilon_{sat} \tag{11}$$

Finally, the tensile test is driven by the relative displacement of the clamps $u(t)$ (displacement-controlled test) so that:

$$u(L_0,t) = \int_0^{L_0} \varepsilon(x,t)dx \tag{12}$$

Another correlated consequence is that spatial resolution of the modelling is expected to be at minimum 2 grain diameters *i.e.* more than 60 μm.

[5] Results presented in the paper have been obtained considering $f(x,t) = f_t(x,t)$, leading to $\dot{f}(x,t) = \dot{f}_t(x,t)$. Indeed flow rule (6) allows to avoid too abrupt transformation rates. But some numerical discrepancies may occur for a macroscopic strain rate $\dot{\delta}/L_0$ close to V_t.

3.4. Update of the thermomechanical constants

Each local thermomechanical constant depends on local phase ratio between Martensite and Austenite. A simple mixture law is employed for thermal expansion coefficient due to 1D serial modelling, and Reuss estimation of Young modulus and thermal conductivity is employed.

$$\alpha(x,t) = f(x,t)\alpha_M + (1 - f(x,t))\alpha_A \tag{13a}$$

$$\frac{1}{E(x,t)} = f(x,t)\frac{1}{E_M} + (1 - f(x,t))\frac{1}{E_A} \tag{13b}$$

$$\frac{1}{\lambda(x,t)} = f(x,t)\frac{1}{\lambda_M} + (1 - f(x,t))\frac{1}{\lambda_A} \tag{13c}$$

E, α and λ are the current Young modulus, the current thermal expansion factor and the current thermal conductivity at position x and time t respectively. X_P represents the X parameter, assumed constant, of the pure P-phase.

3.5. Homogeneous stage

We first consider the direct transformation (from A to M). The reverse case is discussed in the final part of this present paper.

The modelling of the homogeneous transformation is based on the Clausius–Clapeyron diagram plotted in Fig. 7, in which we can define 3 domains separated by the two stress *vs.* temperature transitions, corresponding to onset (M start) and termination (M finish) of the transformation. Upper domain is the martensitic domain, lower domain is the austenitic domain. The intermediate domain is a dual-phase domain ($M + A$). Transitions $\sigma_s(T)$ and $\sigma_f(T)$ are assumed to linearly depend on the temperature exhibiting the same slope K_T (MPa.K^{-1}). The driving force f_t used to calculate the martensitic ratio thanks to Eq. (6) is deduced from the position of a point in the stress–temperature space using a lever rule:

$$\begin{cases} f_t = 0 & \text{if} \quad \sigma < \sigma_s \\ f_t = \frac{\sigma - \sigma_s}{\sigma_f - \sigma_s} & \text{if} \quad \sigma_s \leqslant \sigma \leqslant \sigma_f \\ f_t = 1 & \text{if} \quad \sigma > \sigma_f \end{cases} \tag{14}$$

Nevertheless at this stage we are not able to model the localisation. Indeed a local transformation leads to a local increase of temperature and consequently an increase of σ_s and σ_f that prevents a further transformation in the region. Nucleation and propagation concepts must be introduced.

3.6. Localisation stage

Nucleation and propagation stresses were introduced first by Shaw and Kyriakides (1997). When the nucleation stress σ_n is reached, a pure M band borns. σ_n is higher than the required stress for propagation σ_p. The propagation stress σ_p, is lower than the minimum stress for complete homogeneous martensitic transformation (σ_f). Those stresses appear to linearly depend on the temperature, exhibiting the same slope than σ_s and σ_f transitions. Fig. 7 illustrates the homogeneous domain (as described in Section 3.5) and the so-called nucleation and propagation stresses *vs.* temperature transitions.

The propagation laws can be summarized as follows:

i. When the stress reaches the nucleation stress at any point, then this point is "nucleated",
ii. When any point (or its neighbourhood) is nucleated *AND* when the stress is higher than propagation stress, this point is submitted to propagation,

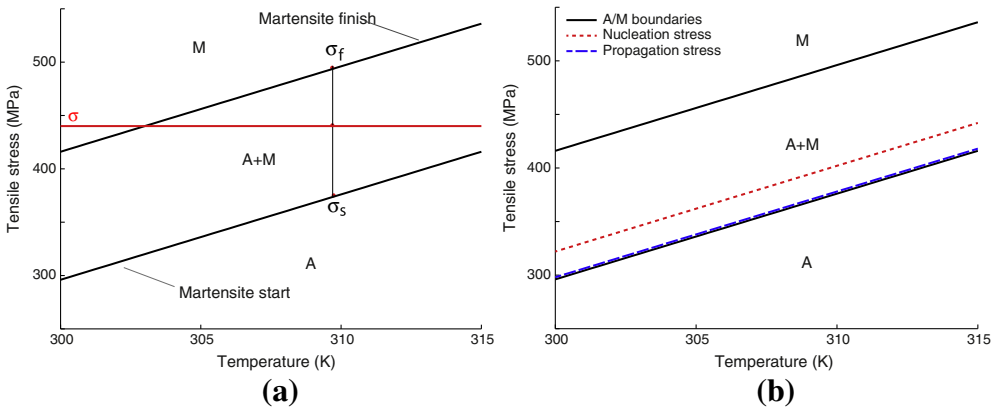

Fig. 7. (a) Clausius–Clapeyron diagram and associated lever rule. (b) Homogeneous and localisation boundaries for the direct transformation: from *A* to *M* phases.

iii. When any point (or its neighbourhood) is submitted to propagation at any time step *AND* when the stress is higher than the propagation stress at the next time step, this point is submitted to propagation at the further step.

These rules are written mathematically using boolean operators:

$$N(x,t) = [\sigma(t) > \sigma_n(x,t)] \tag{15a}$$

$$P(x,t) = (N(x \pm dx, t) \vee P(x \pm dx, t-dt)) \wedge [\sigma(t) > \sigma_p(x,t)] \tag{15b}$$

$\vee$ et $\wedge$ being the boolean operators *OR* and *AND* respectively, and $[\cdot]$ being the predicate ($[h] = 1$ if h is true, 0 else). N denotes the nucleated state whereas P is the propagation undergoing. $\pm dx$ denotes here the near region of x:

$$N(x \pm dx, t) = N(x,t) \vee N(x+dx,t) \vee N(x-dx,t)$$

$$P(x \pm dx, t) = P(x,t) \vee P(x+dx,t) \vee P(x-dx,t)$$

dx and dt are the element size and the time step respectively. The definition of the neighbourhood appears to make this model theoretically mesh dependent (influence of the values of dx and dt), but we will figure out later (part 5) that this assumption is false.

f_t takes now two possible values depending on $P(x,t)$:

$$\begin{cases} \text{if } P(x,t) \text{ is false} & \Rightarrow \quad f_t(x,t) \text{ is calculated from Eq. (14)} \\ \text{if } P(x,t) \text{ is true} & \Rightarrow \quad f_t(x,t) = 1 \end{cases} \tag{16}$$

The introduction of a nucleation stress different from the propagation stress is a practical way to take into account the local stress concentration due to the local appearance of variants of (M) that are not fully compatible with the (A) parent phase. Indeed the model is one-dimensional that does not allow to define such a stress gradient.

4. Numerical algorithm

The equations introduced above lead to a strong non-linear problem, especially because of the transient thermal phenomenon. A numerical code has been implemented.

4.1. Thermal solver

A Backward Euler Finite Difference decomposition of the sample has been done (Rappaz et al., 2003). X_j^n denotes the value of X in the element $j \in [1,m]$ (m being the number of elements) at the time step n. F^n is the vector corresponding to the local heating and T^n the vector corresponding to the temperature of each element. The decomposition of Eq. (4) gives the following implicit matrix system:

$$\begin{bmatrix} (C^n) & ({}^tBC^n) \\ (BC^n) & 00 \\ & 00 \end{bmatrix} \begin{Bmatrix} T_1^{n+1} \\ T_2^{n+1} \\ \vdots \\ T_m^{n+1} \\ \alpha^n \\ \beta^n \end{Bmatrix} = \begin{Bmatrix} T_1^n \\ T_2^n \\ \vdots \\ T_m^n \\ T_{clamp} \\ T_{clamp} \end{Bmatrix} + \begin{Bmatrix} F_1^n \\ F_2^n \\ \vdots \\ F_m^n \\ 0 \\ 0 \end{Bmatrix} \tag{17}$$

Where $[C]^n$ is the $m \times m$- thermal inertia matrix, $[BC]^n$ the $2 \times m$-additional matrix for the Lagrange Multiplier due to boundary conditions (5):

$$[C]^n = \begin{bmatrix} A_1 & -B_1 & 0 & \cdots & 0 & 0 \\ -B_2 & A_2 & -B_2 & \ddots & & 0 \\ 0 & -B_3 & A_3 & \ddots & \ddots & \vdots \\ \vdots & \ddots & \ddots & \ddots & -B_{m-2} & 0 \\ 0 & & \ddots & -B_{m-1} & A_{m-1} & -B_{m-1} \\ 0 & 0 & \cdots & 0 & -B_m & A_m \end{bmatrix}$$

With:

$$A_1^n = A_m^n = 1 + \frac{h\ell dt}{S_0 \rho C_p} \quad \text{and} \quad A_i^n = 1 + \frac{h\ell dt}{S_0 \rho C_p} + \frac{2\lambda_i^n dt}{\rho C_p dx^2} \tag{18a}$$

$$B_1^n = B_m^n = 0 \quad \text{and} \quad B_i^n = \frac{\lambda_i^n dt}{\rho C_p dx^2} \tag{18b}$$

$$F_i^n = \Delta H \frac{f_i^n - f_i^{n-1}}{C_p} + \frac{h\ell dt T_{air}}{S_0 \rho C_p} \tag{18c}$$

$$[BC]^n = \begin{bmatrix} 0 & 0 & 0 & \dots & 0 & \frac{-\lambda_m^n}{h_c dx} & 1 + \frac{\lambda_m^n}{h_c dx} \\ 1 + \frac{\lambda_1^n}{h_c dx} & \frac{-\lambda_1^n}{h_c dx} & 0 & \dots & 0 & 0 & 0 \end{bmatrix} \tag{18d}$$

4.2. Martensite ratio evolution

Numerical resolution of the flow Eq. (6) gives:

$$f(x, t+dt) = V_t dt (f_t(x,t) - f(x,t)) + f(x,t) \tag{19}$$

This formulation is not used if we choose $f(x,t) = f_t(x,t)$. This simplification has been considered in the numerical applications.

4.3. Algorithm

The numerical code associated to the model can be described by the flowchart given in Fig. 8. The initial temperature is considered as a constant, denoted T_{ini}. For each time step n, the elastic displacement (u_{el}) is calculated with the total displacement (u) and the inelastic displacement (due to phase transformation):

$$u_{el}^n = u^n - \sum_{i=1}^{m} f_i^n \varepsilon_{sat} dx \tag{20}$$

The local Young moduli are calculated from Eq. (13b). Since homogeneous stress hypothesis is used (1D problem), a Reuss estimation of the global equivalent Young modulus (E_{eq}) is computed:

$$\frac{1}{E_{eq}^n} = \sum_{i=1}^{m} \frac{1}{E_i^n} \tag{21}$$

The stress is calculated from the macro elastic strain and the equivalent Young modulus:

$$\sigma^n = E_{eq}^n \frac{u_{el}^n}{L_0} \tag{22}$$

Typical results are reported in the next sections for $dx = 240\ \mu m$ (500 elements).

5. Simulation results and comparison to experimental data

5.1. Algorithm and identification of thermal parameters

The algorithm described on Fig. 8 has been implemented using Matlab. Tables 1–3 give the parameters used for the simulations. The values of parameters and material constants

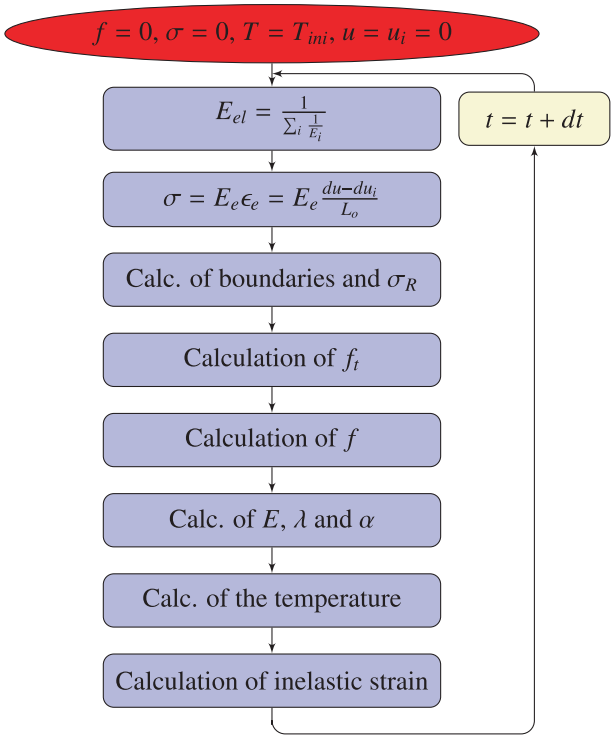

Fig. 8. Numerical algorithm for the resolution of the equations associated to the model.

($C_p, \lambda_A, \lambda_M, \Delta H \ldots$) provided by the material supplier, in agreement with different sources in the literature (however, the values slightly vary from one author to another). The geometrical parameters correspond to the experimental set up reported in Section 2.1. The external thermal parameters (h, h_c) were chosen in order to properly fit the experimental data provided in Section 2.2. The value used for the slope of $\sigma(T)$ transition in the Clausius–Clapeyron diagram is K_T = 8 MPa K^{-1} in agreement with Shaw and Kyriakides (1997). Temperatures reported in Table 3 correspond to temperatures T_i of homogeneous and localisation boundaries i reported in Fig. 7 at zero stress so that:

$$\sigma_i(T) = K_T(T - T_i) \tag{23}$$

An arbitrary stress concentration can be used in order to model a distribution of defects (of geometrical, crystallographic or thermal origin) that initiate the transformation bands:

$$\sigma_{eff}(x,t) = (1 + \zeta\Omega(x))\sigma_{th}(t) \tag{24}$$

σ_{eff} denotes the effective stress, used for the driving force calculation, whereas σ_{th} is the theoretical stress, uniform over the length, calculated from the elastic strain. ζ is the nominal defect and Ω is a random value taken between $]-1,1[$. It must be noted that such localisation parameter is not necessary since the thermal heterogeneity is sufficient to initiate nucleation of the bands. In the following simulations, ζ has been fixed at 0. A study of sensitivity to this parameter is nevertheless reported in Section 5.4.

Fig. 9(a–f) and 10(a–d) allow one to compare the experimental data reported in Section 2.2 using the IRIC system to the modelling results for $\dot{\delta}/L_0 = 4.2 \times 10^{-4}$ s^{-1} and $\dot{\delta}/L_0 = 8.3 \times 10^{-5}$ s^{-1} respectively. The experimental spatiotemporal maps are not available for the second test. The area of measurement is limited to 40x26 mm^2 in the center region of specimen.

Fig. 9(b) shows the stress–strain curve obtained to be compared to Fig. 9(a) (Fig. 10(a) and (b) respectively). The first linear stage (0-) is due to perfect austenite elasticity. The second stage (-) is the homogeneous transformation. At the point , a first localisation occurs and propagates until , only visible for the low strain rate test. From to the end, the transformation is almost complete and the increase of stress is associated to martensite elasticity. These results highlight the influence of the strain rate on both homogeneous and propagation stages.

Whereas Figs. 9(b) and 10(b) only show the macroscopic behaviour (mean strain calculated from the relative displacement of the two clamps), Figs. 9(d) and (f), and 10(c) and (d) give the map corresponding to the evolution of axial deformation and temperature along the sample at each step corresponding to the simulation of Figs. 9(b) and 10(b). The colour indicates the level of the corresponding variable at each position on the sample (ordinate) and at any time (abscissa). Fig. 9(c) and (d) (9(e) and (f) respectively) show a good adequacy between the experimental and the modelled spatiotemporal maps: correlation in time, strain level, temperature level and space between bands (one must remember that full field is not reachable by experimental set-up).

These figures are completed with Fig. 11 exhibiting the martensite ratio in the same spatiotemporal frame for both experiments. During the elastic stage (0-), no martensite is created. Hence, only thermoelasticity could be taken into account for the temperature evolution. The strain rate is small so that the sample is almost isothermal during this stage. The homogeneous transformation starts at the same time in the whole sample. Due to boundary conditions (T_{clamp}) and exothermic transformation, the lowest temperature stays at the clamps whereas the highest is reached in the middle of the sample during the homogeneous transformation. As a result of this temperature gradient, the first occurrence of the nucleation stress is always at the clamps: the two first bands born consequently on the top and the bottom of the sample. Then,

Table 1
Geometrical and external parameters for simulation.

Outside temp.	Init. temp.	Init. length	Cross sect.	Out. length	Conv. factor	Conductance
$T_{air} = T_{clamp}$	T_{ini}	L_0	S_0	ℓ	h	h_c
290	290	120	40	46	10	500
K	K	mm	mm^2	mm	$Wm^{-2}K^{-1}$	$Wm^{-3}K^{-1}$

Table 2
Material parameters.

Th. capacity	Thermal conductivities		Young moduli		Th. expansion factors		Latent heat	Density
C_p	λ_A	λ_M	E_A	E_M	α_A	α_M	ΔH	ρ
322	18	8.6	32.5	31.5	11×10^{-6}	6.6×10^{-6}	9,000	6,500
$J\,kg^{-1}K^{-1}$	$Wm^{-1}K^{-1}$	$Wm^{-1}K^{-1}$	GPa	GPa	K^{-1}	K^{-1}	$J\,kg^{-1}$	$kg\,m^{-3}$

Table 3
Temperature of homogeneous and localisation boundaries of Clausius–Clapeyron diagram (Fig. 7).

Martensite start	Martensite finish	Nucleation temp.	Propagation temp.
M_s	M_f	M_n	M_p
263	248	259.75	262.75
K	K	K	K

the temperature at the fronts of the bands increases as well as the stress required for the propagation. Considering the thermal exchange, stress becomes high enough before the arrival of the bands in the middle part of the sample so a new nucleation occurs at the lowest-temperature point. A lower thermal exchange parameter or lower strain rate would lead to the birth and propagation of only one band. We meet the condition of multiple bands without propagation at high strain rate or low thermal exchange. The same phenomena have been experimentally described in Shaw and Kyriakides (1997).

As a first conclusion, we observe a satisfying agreement between the experiments and the modelling: stress/deformation levels, number of bands,[6] associated strain and temperature levels.

5.2. Validation

The thermal parameters have been chosen in order to properly qualify the IRIC experiment. Figs. 9 and 10 do not constitute a validation of the approach. Other comparisons are required involving different strain rates and geometries. This point is addressed in this paragraph.

The same material is used for this new experimental campaign. The section is still rectangular but width and thickness are different leading to a different heat exchange (section = 12 $\times$ 2.5 mm^2). The gauge length is kept as 120 mm long. The deformation ratio chosen are: $\dot{\delta}/L_0 = 2.8 \times 10^{-5}$; $2.8x10^{-4}$ s^{-1}. During the tests, room temperature is now 23 ± 0.5°C. Fig. 12 illustrates the stress–strain curves obtained for experiments and modelling. The following discrepancies can be observed: the stress threshold is overestimated of about 50 MPa. At the lower strain rate, the model predicts a stress plateau which is not observed in the experiment. The stress drop is to be related to shift between stress germination and stress propagation. The one-dimensional model inevitably leads to this kind of result. On the other hand the model does not allow to understand for such phenomena as the knee observed at 60 MPa in the experimental results. It is recalled that austenite to *R*-phase transformation is not taken into account in the model. This transformation is indeed normally not active since the intensity of the chemo-mechanical coupling is reduced due to the low transformation strain associated with *R*-phase. However it is possible as mentioned in the introduction that the material in the initial state is biphasic $R-A$. Such an environment and associated internal stresses can promote the occurrence of a small amount of *R*-phase at low stress level, giving rise to such non-linearity.

These results are complemented by the associated spatiotemporal maps, *i.e.* martensite ratio and temperature for modelling, and axial deformation for experiments and modelling. Fig. 13 allows to compare experimental to modelled axial deformation, exhibiting the localisation bands. The number of bands is in good agreement between experiments and modelling: two bands at low strain rate; five bands for experiment and modelling at high strain rate (three visible in the area of observation and two bands at the clamps); strain levels....

Modelling results concerning martensite ratio and associated temperature elevation are reported in Fig. 14. The comment is the same as with previous simulations. The strain rate remains small so that thermoelasticity is not perceptible or masked by the thermal emission due to the homogeneous transformation stage. Whatever the test, the transformation begins at the clamps.

At a low strain rate (Fig. 14(a)), only two bands occur and propagate. We meet the condition of multiple bands without propagation at high strain rate.

These few experimental results and associated modelling confirm that the localisation phenomenon is suitably described by the model. Comparisons at higher strain rate require experiments that are difficult to process. Results reported in the next section allow us to conclude to the ability of the model to predict the number of bands, stress and strain level in a wide range of strain rate.

5.3. Influence of loading conditions on the localisation phenomenon

In Zhang et al. (2010), authors have attempted to reveal the roles of strain rate, conductivity and heat convection coefficients in controlling the number of bands and spacing. For most NiTi polycrystals and heat transfer boundary conditions, the maximum domain number n_{max} increases with increasing applied nominal strain rate $\dot{\varepsilon}$ and decreases with increasing heat convection and conductivity. A simple relationship between strain rate and number of bands, in two different cases, has already been established (Zhang et al., 2010; He and Sun, 2010):

$$n_{max} = C\dot{\varepsilon}^m \tag{25}$$

[6] Area of measurement is positioned at the centre of the specimen; it is too small to observe bands coming from clamps.

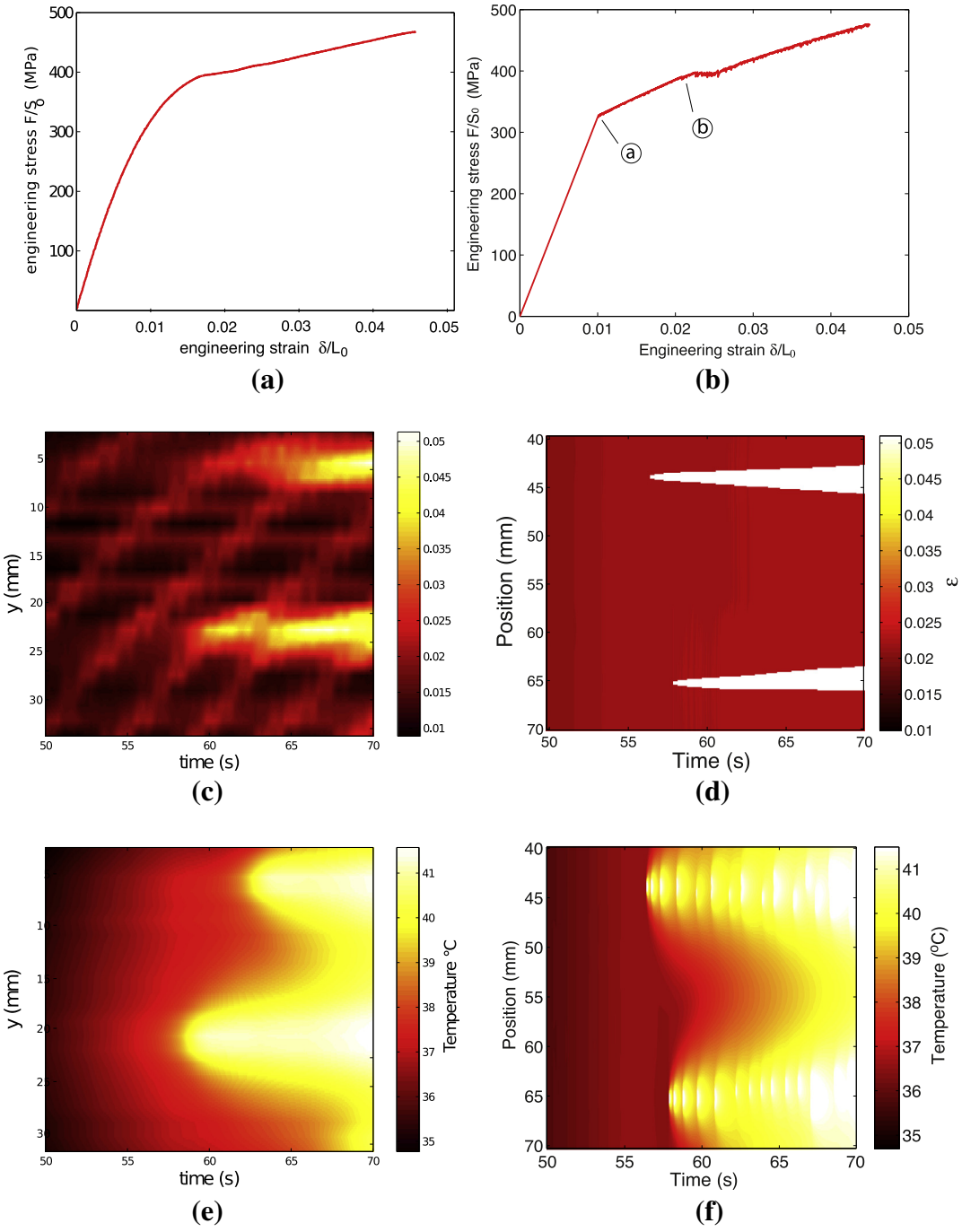

Fig. 9. Comparison experiments/ modelling: a/b- tensile curves at $\dot{\delta}/L_0 = 4.2 \times 10^{-4}\ s^{-1}$. c/d- spatiotemporal map of axial deformation. e/f- spatiotemporal map of temperature. Dimensions are given in mm.

- For the case of no convection, a simple square root relationship ($m = 0.5$) between maximum number of bands and strain rate is obtained.
- For the case of a very large convection, the number of bands is proportional to the strain rate ($m = 1$).

Some simulations have been performed using several strain rates, but with the same thermal conditions (the convection coefficient chosen as representative of the tests is $h = 10\ Wm^{-2}\ K^{-1}$). Fig. 15 reports a typical result of simulation for a much high strain rate than previous tests ($\dot{\delta}/L_0 = 1.4 \times 10^{-2}\ s^{-1}$) illustrating the so-called multiple bands phenomenon. The stress–strain curve exhibits a high slope with oscillations at the point of nucleation of the bands (illustrated in Fig. 16 where time variation of average quantities are plotted). Spatiotemporal maps indicate a large number of bands with a high elevation of temperature. Considering the unexpected enlargements of the bands, a possible effect of the number of elements (spatial discretisation) on the result is highlighted.

Many other strain rates (5 decades) have been tested using 500, 1000 and 2000 elements to address the role of discretisation. Fig. 17 shows the evolution of the number of localised bands, got from all the simulations.

At lower strain rate, the number of bands reaches the asymptotic value of 1 (nucleation at a clamp) after a long saturation at

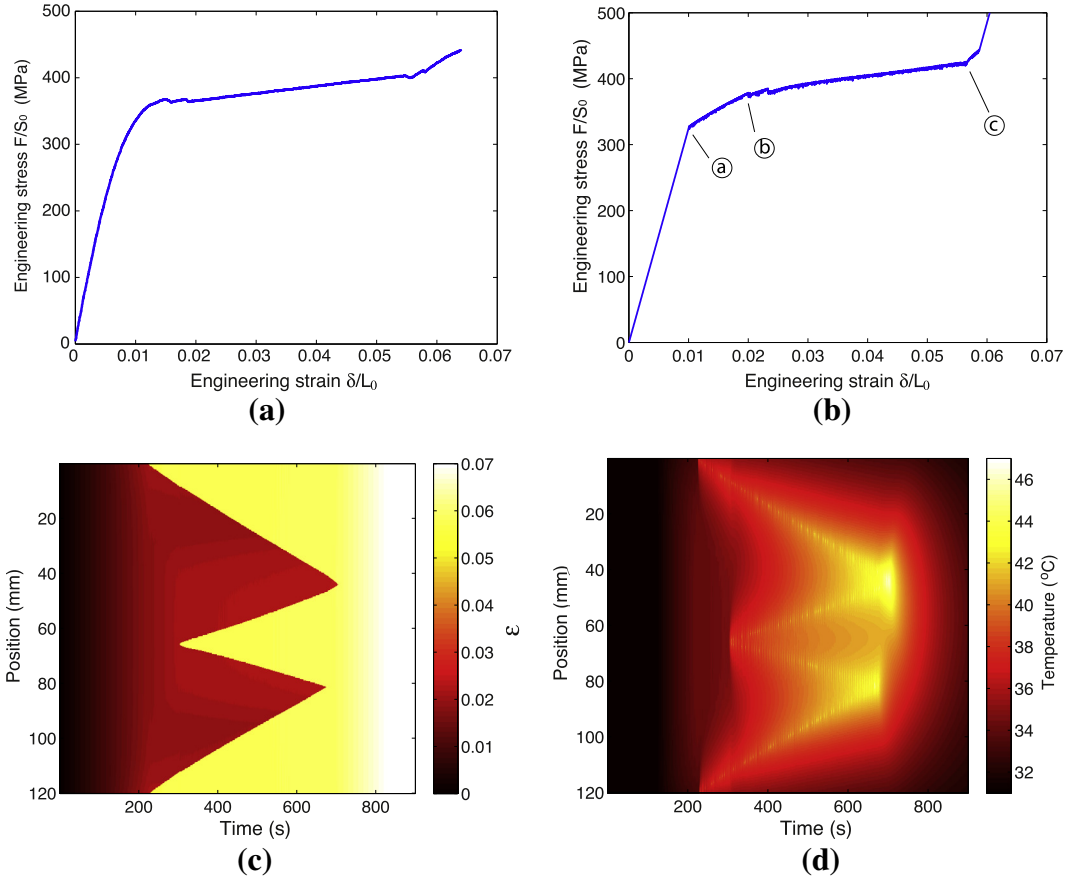

Fig. 10. Comparison experiments/ modelling: a/b- tensile curves at $\dot{\delta}/L_0 = 8.3 \times 10^{-5}$ s^{-1}. c- spatiotemporal map of axial deformation. d- spatiotemporal map of temperature. Dimensions are given in mm.

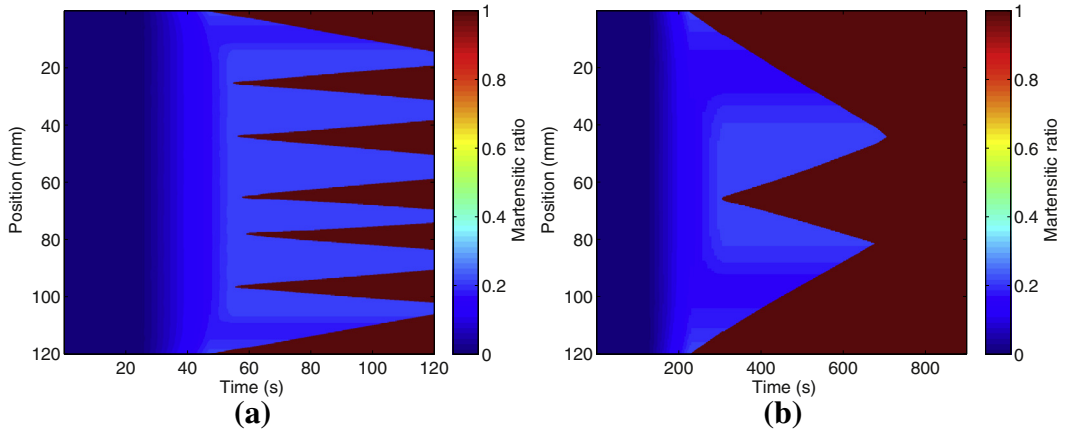

Fig. 11. Modelling: spatiotemporal map of martensite ratio corresponding to IRIC test at: (a) $\dot{\delta}/L_0 = 4.2 \times 10^{-4}$ s^{-1}; (b) $\dot{\delta}/L_0 = 8.3 \times 10^{-5}$ s^{-1} .

2 bands. At higher strain rate, a limit appears dependent on discretisation. We observe a saturation at 35 bands for 500 elements. This limit reaches 55 bands for 1000 elements. The limit is extended to much higher value with the use of 2000 elements. A linear variation of number of bands *vs.* strain rate is observed in the log–log diagram. The linear regression gives a good correlation coefficient (R = 0.975) for the points considered and its slope is 0.452. The number of bands and the strain rate can be approximately linked using the relationship:

$$N = 229.5(\dot{\delta}/L_0)^{0.452} \tag{26}$$

This result is quite close to the relation established in Shaw and Kyriakides (1995) and in Zhang et al. (2010) more recently, in accordance with the low convection condition ($h = 6.5$ Wm^{-2} K^{-1} in Shaw and Kyriakides (1995)). C represents the maximum number of bands at $\dot{\delta}/L_0 = 1$ s^{-1}. The parameters used lead to $C \simeq 229s^m$ (Fig. 17). This number must be compared to the number of elements: the number of elements should be much larger than the number of potential bands for nucleation, leading to a lower bound for the number of elements at a given strain rate. This point is illustrated by Fig. 18, where the number of bands is plotted as a function of number of elements at high strain rate

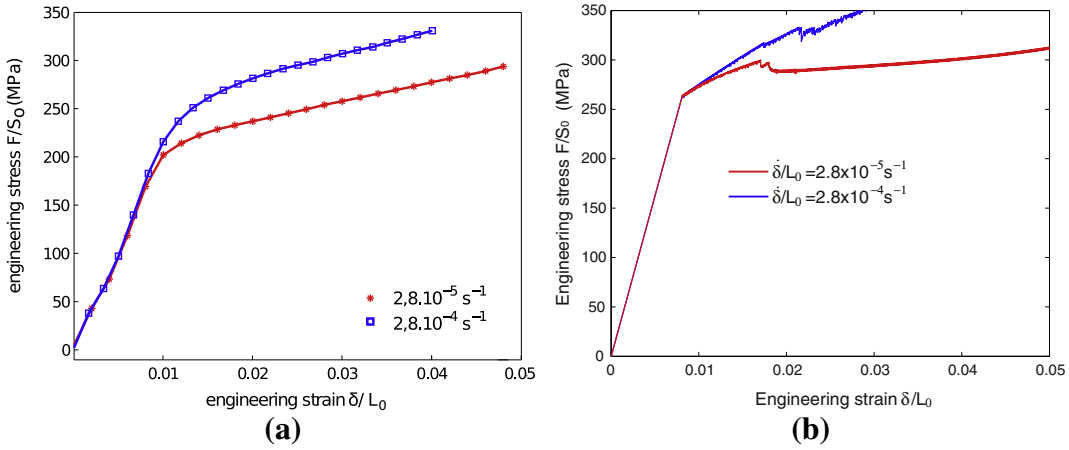

Fig. 12. Comparison experiments/ modelling: a/b- tensile curves at $\dot{\delta}/L_0 = 2.8 \times 10^{-5}; 2.8 \times 10^{-4}$ s^{-1}.

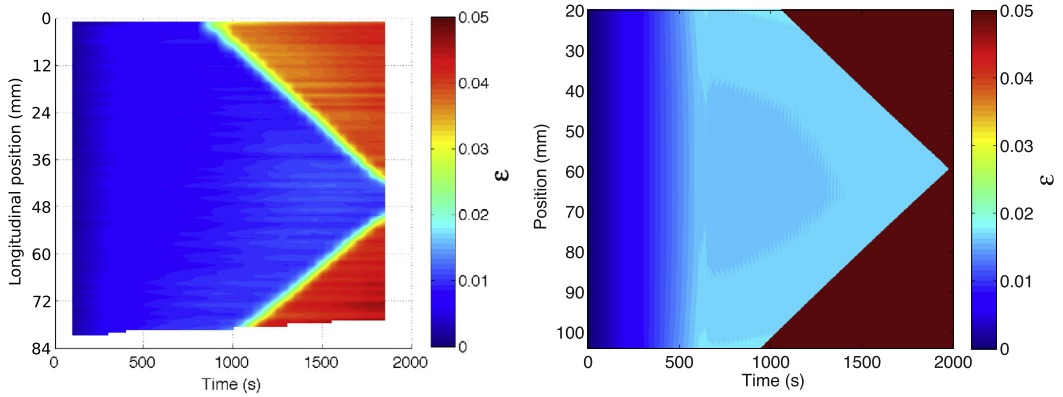

(a) $\dot{\delta}/L_0$=2.8x10^{-5} s^{-1}

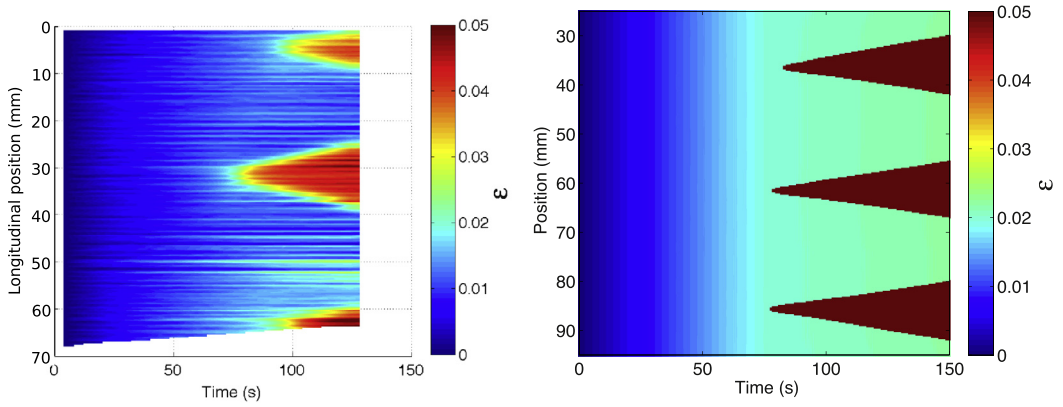

(b) $\dot{\delta}/L_0$=2.8x10^{-4} s^{-1}

Fig. 13. Comparison experiments/ modelling of spatiotemporal evolution of the axial deformation at different strain rates for the exact same thermal conditions and geometries.

($\dot{\delta}/L_0 = 1.4 \times 10^{-1}$ s^{-1}). Number of bands drastically decreases to 2 for number of elements lower than 250 as a clear threshold. For number of elements higher than 250, the number of bands progressively reaches its maximal value.

Other authors recommended to introduce the strain gradient (Shaw, 2002; Chang et al., 2006) which regularises the localisation. But sensitivity to mesh still remains. On the other hand, these models cannot properly take the homogeneous transformation into account.

5.4. Sensitivity to convection and defect coefficients

Different heat coefficients have been implemented in the 1D-modelling in order to cross the theoretical approach of Zhang et al. (2010). It has been verified that higher convection coefficients lead to an increase of the exponent m and a decrease of C joining the analytical approach. Fig. 19 shows the nucleation of bands obtained at $\dot{\delta}/L_0 = 2.8 \times 10^{-4}$ s^{-1} for two extreme convection coefficients h (0.1 Wm^{-2} K^{-1} and 1000 Wm^{-2} K^{-1}) to be compared to

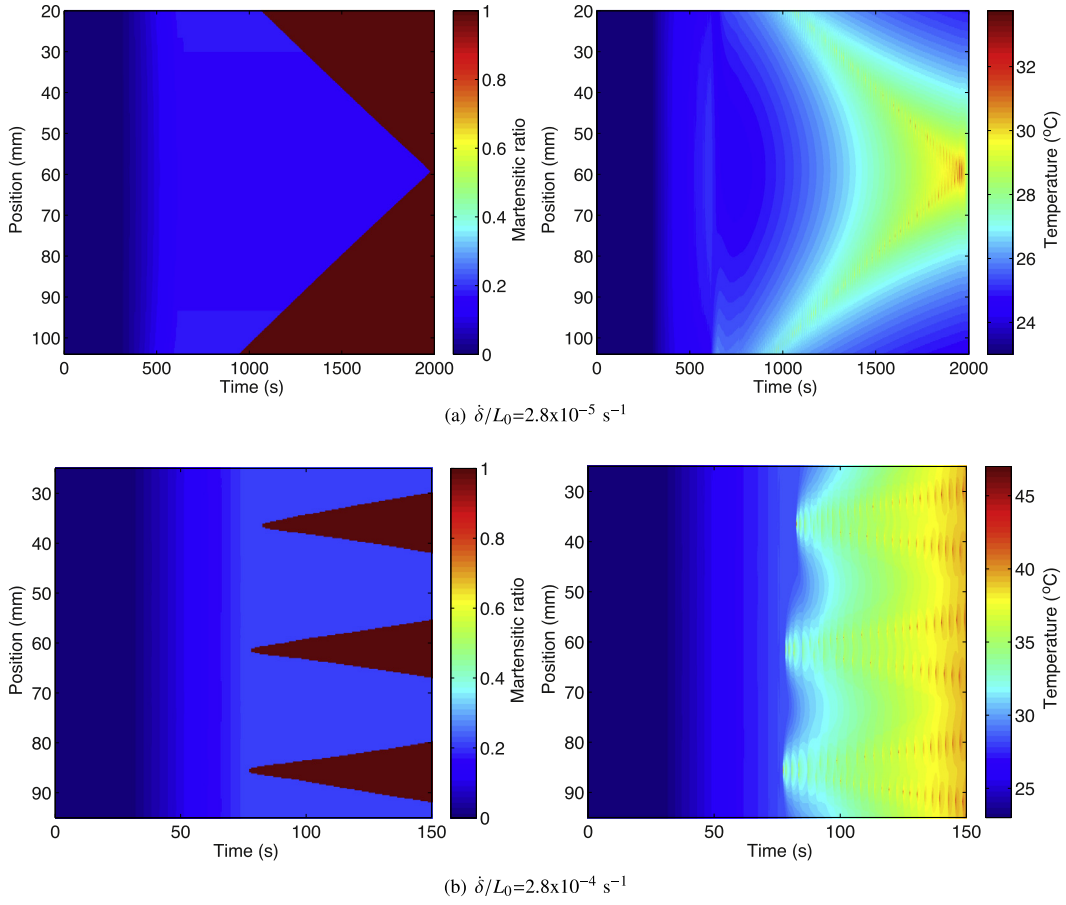

Fig. 14. Modelling results: spatiotemporal evolution of the martensite volume ratio f and of the temperature T(Celcius degrees) at different strain rates for the exact same thermal conditions.

Fig. 13(b) obtained for the same strain rate and for $h = 10\ \mathrm{Wm^{-2}\ K^{-1}}$. The number of bands for $h = 0.1\ \mathrm{Wm^{-2}\ K^{-1}}$ is the same as for $h = 10\ \mathrm{Wm^{-2}\ K^{-1}}$ indicating that $10\ \mathrm{Wm^{-2}\ K^{-1}}$ already corresponds to low convection situation. High convection modelling is quite close to modelling implemented at low strain rate with a reduced number of bands. Fig. 20 shows the evolution of the number of localised bands at different strain rates for convection coefficients $h = 0.1\ \mathrm{Wm^{-2}\ K^{-1}}$ and $h = 1000\ \mathrm{Wm^{-2}\ K^{-1}}$ for a 2000 elements discretisation, and associated linear approximations. The change of slope is clearly highlighted (from 0.45 to 0.8 meeting the boundary coefficients proposed by Zhang et al., 2010 and He and Sun, 2010). High convection leads to a delay of nucleation at low strain rate before curves join for strain rate higher than $\dot{\delta}/L_0 \approx 3 \times 10^{-3}\ \mathrm{s^{-1}}$, where convection becomes negligible compared to conduction. The strain rate domain where Eq. (25) is valid strongly depends on the convection condition: at lower convection, a conduction-controlled nucleation is observed, leading a power law correlation on a wide range of strain rate; at higher convection, a transition is clearly observed from convection to conduction - controlled nucleation, leading to a sharp change of power law coefficient.

Fig. 21 illustrates the effect of defect parameter ζ on the initiation of bands. The modelling has been implemented at lower strain rate $\dot{\delta}/L_0 = 1.4x10^{-5}\ \mathrm{s^{-1}}$ using the usual convection conditions ($h = 10\ \mathrm{Wm^{-2}\ K^{-1}}$). Below 0.035, the defect parameter has no significant role; for a value higher than 0.04, the number of bands drastically increases as illustrated in Fig. 22. Bands initiated by defects present a much more complex structure than the multi band system usually observed at high strain rate.

Another discussion point concerns the role of gap between nucleation stress and propagation stress. It is not clear how this gap, as a structural parameter (not intrinsic parameter), acts on the expression for the strain rate dependence of number of bands (24). The physical justification of this energy is classic: as any phenomenon of germination, the stability of such a process depends on the ratio between the volume energy (free energy) and the surface energy (surface tension, boundary phenomena). The stability of a band can be interpreted in the same way. Crossing Clapeyrons lines gives the potential energy necessary for the formation of martensite. The formation of a band requires higher energy, which is very dependent on the specimen geometry. It is therefore understandable that the gap between propagation stress and nucleation stress depends on the specimen geometry. One can reasonably ask the question of the dependence of the parameters of the relationship between the number of bands and strain rate for this phenomenon. The chosen geometries considered in experiments are too close to allow an experimental analysis of this point. However, the model can help to observe the changes in the relationship between the number of bands and strain rate for different nucleation thresholds. The influence of the ratio between nucleation and propagation stresses has been evaluated, nucleation stress ranging from a value close to the propagation stress value (small gap) at a stress value close to the maximum threshold (large gap) and considering quasi-adiabatic condition ($h = 0.1\ \mathrm{Wm^{-2}\ K^{-1}}$). Fig. 23 shows the evolution of the number of bands as a function of the strain rate for seven different levels of nucleation stress. κ factor defined by Eq. 27 has been introduced for that purpose: κ values vary from 0 to 1.

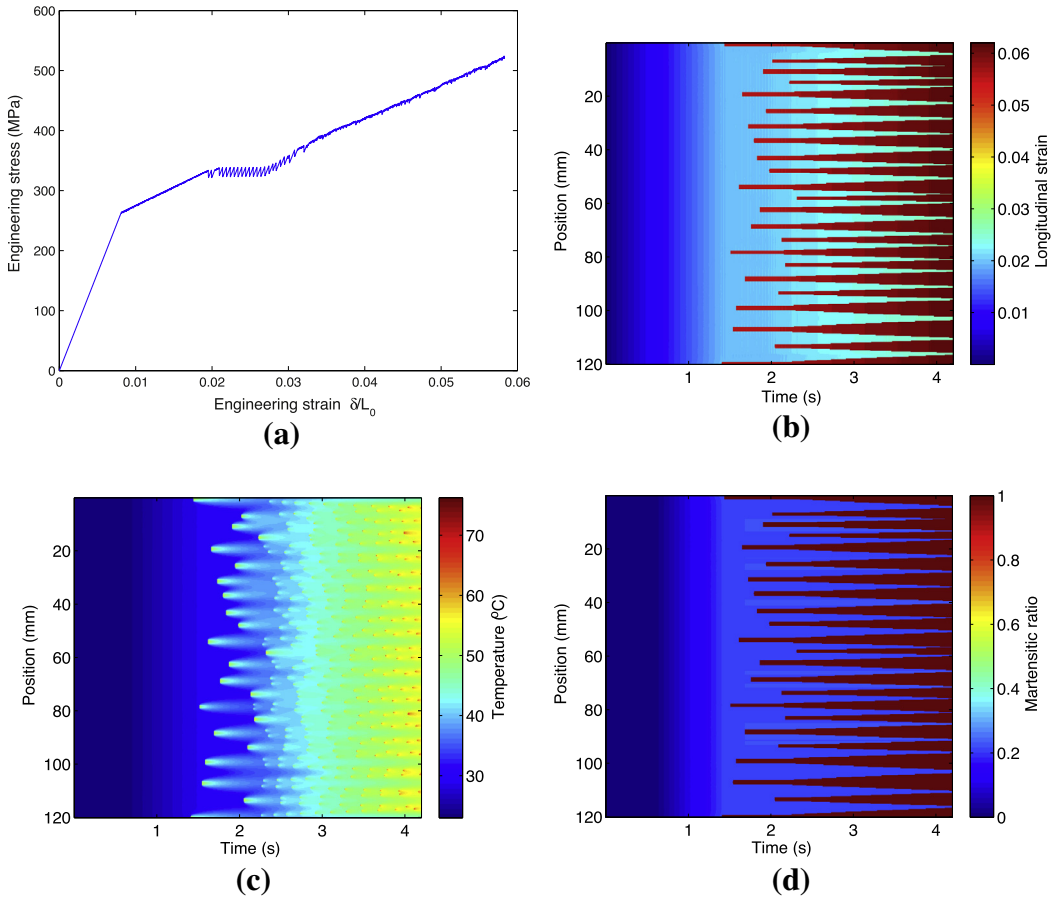

Fig. 15. Modelling results at $\dot{\delta}/L_0 = 1.4 \times 10^{-2}\ s^{-1}$: a-Engineering stress–strain curve; b/c/d spatiotemporal evolution of the longitudinal strain ε, temperature T(Celsius degrees), and of the martensite volume ratio f.

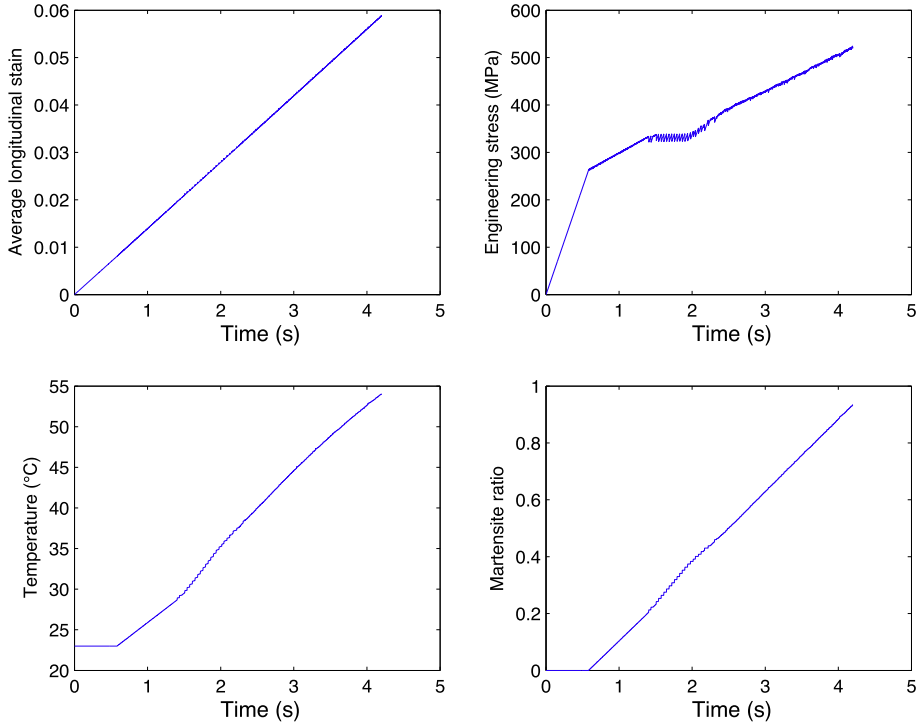

Fig. 16. Modelling results at $\dot{\delta}/L_0 = 1.4 \times 10^{-2}\ s^{-1}$: variation of engineering stress and strain, average temperature and martensite ratio as function of time.

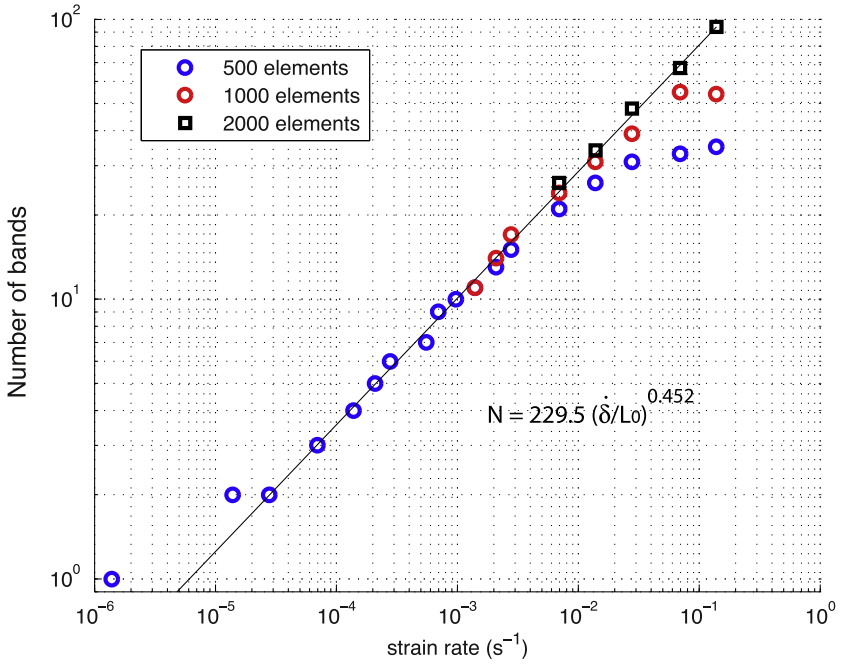

Fig. 17. Number of localized band (N) *vs.* strain rate ($\dot{\delta}/L_0$) in a log–log grid.

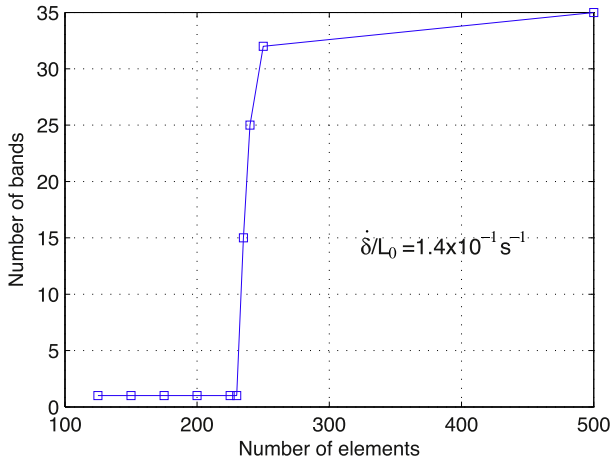

Fig. 18. Effect of number of elements on number of bands.

$$\kappa = \frac{\sigma_{nucleation} - \sigma_s}{\sigma_f - \sigma_s} = \frac{M_n - M_s}{M_f - M_s} \tag{27}$$

The simulation for high nucleation stress (physically unrealistic) requires a strong discretization of the medium (4000 to 6000 elements, 7000 time steps) to avoid mesh sensitivity. For a better analysis, some fitting curves (corresponding to power law $C = \dot{\varepsilon}^m$ whose exponent m is set to 0.5) have been added. A good agreement between fitting laws and numerical points is observed. This seems to demonstrate that the exponent 0.5 is a constant independent of the nucleation stress and consequently independent of the specimen geometry. Constant C is conversely dependent on the geometry. Optimised C values are plotted in Fig. 24 as function of κ in a semi-log graph.

The variation of C *vs* κ may be represented by a relationship close to an Arrhenius equation according to:

$$C = C_0 exp\left(-\frac{\kappa}{r}\right) \tag{28}$$

with $C_0 = 620\ s^{0.5}$ and $r = 0.435$. κ acts as an activation energy.

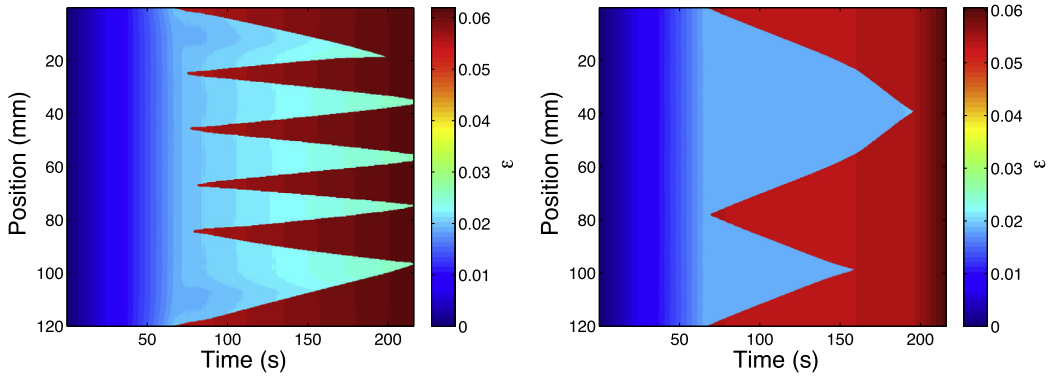

(a) h=0.1 $Wm^{-2}K^{-1}$ (b) h=1000 $Wm^{-2}K^{-1}$

Fig. 19. Spatiotemporal evolution of the longitudinal strain at $\dot{\delta}/L_0 = 2.8 \times 10^{-4}\ s^{-1}$: a- low convection coefficient; b- high convection coefficient.

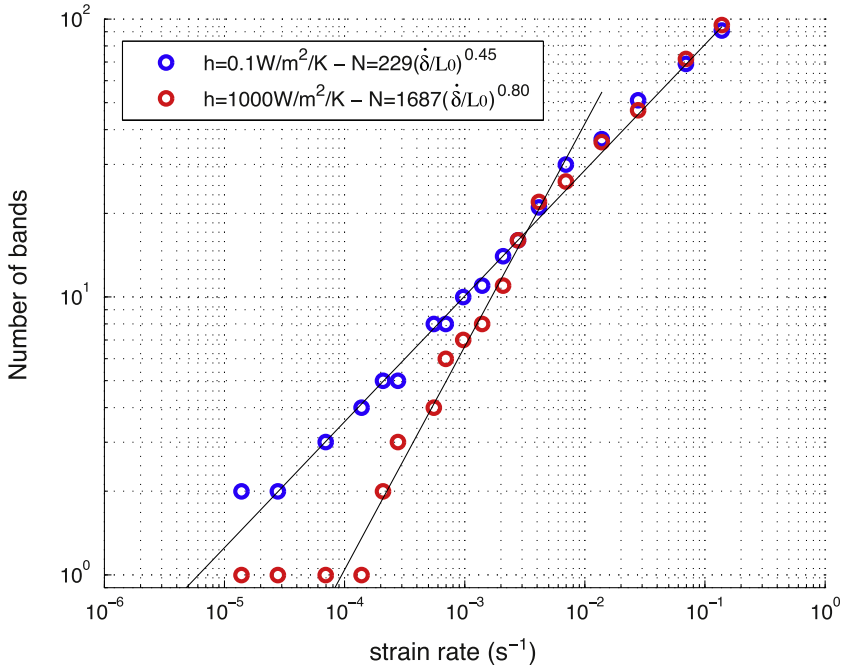

Fig. 20. Number of localised band (N) *vs.* strain rate ($\dot{\delta}/L_0$) in a log–log grid for two extreme convection conditions.

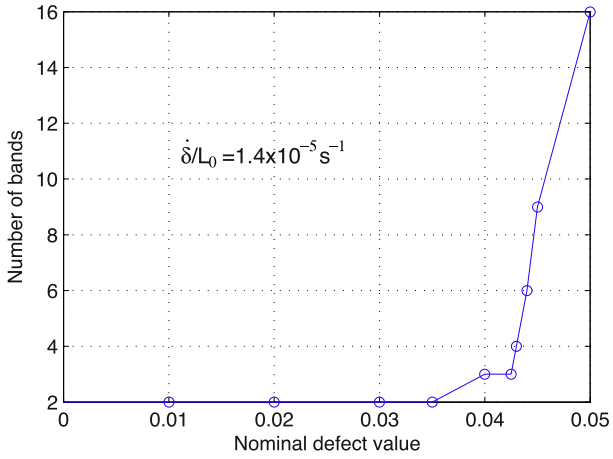

Fig. 21. Effect of parameter ζ as defect parameter on number of bands.

Obviously such purely numerical observations should be completed by experimental observations. But setting up tests with identical convection coefficient for very different geometries is a difficult challenge to overcome.

6. Toward the modelling of the hysteresis

6.1. Forward and reverse transformations

All the considerations detailed above only deal with transformation $A \rightarrow M$. Experimental results (Fig. 3) show that the reverse phenomenon ($M \rightarrow A$ transformation) occurs during the unloading (austenitic transformation is endothermic, and localisation appears) leading to a mechanical hysteresis. Hence, we have to define new transformation boundaries in the Clausius–Clapeyron diagram:

- σ_{ms} and σ_{mf} : stresses corresponding to M start and finish (forward homogeneous transformation),

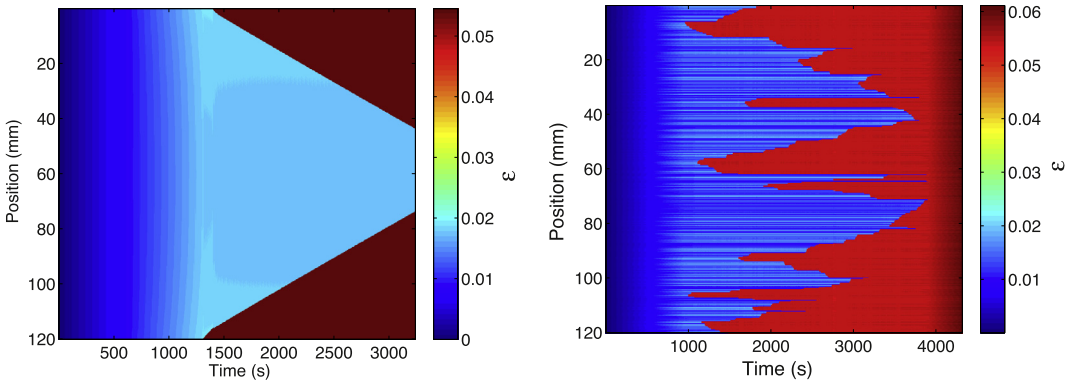

(a) ζ=0 (b) ζ=0.044

Fig. 22. Illustration of bands for two different values of parameter ζ.

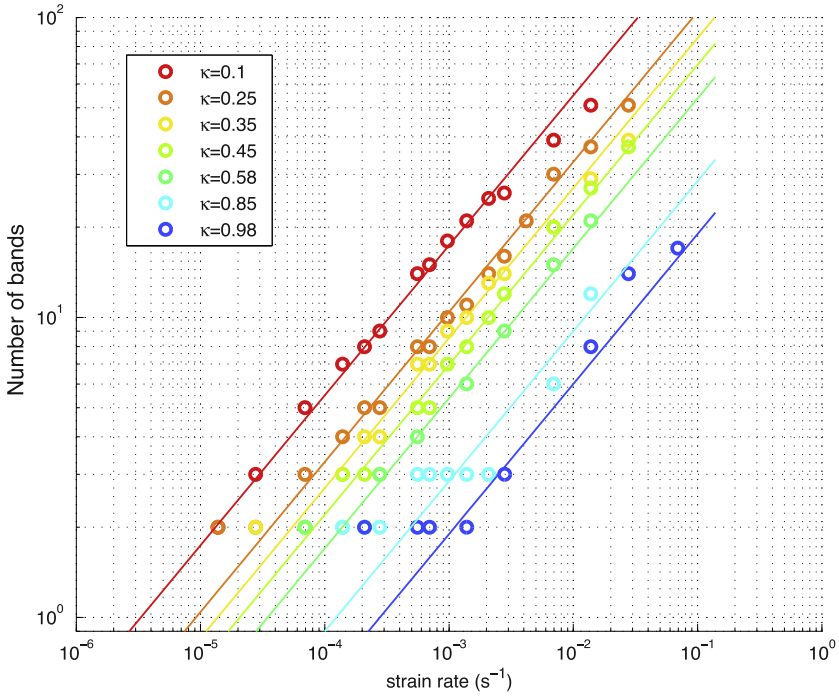

Fig. 23. Number of localised band (N) *vs.* strain rate ($\dot{\delta}/L_0$) in a log–log grid for various nucleation conditions (κ).

- σ_{mn} and σ_{mp} : stresses corresponding to M nucleation and propagation (forward localised transformation),
- σ_{as} and σ_{af} : stresses corresponding to A start and finish (reverse homogeneous transformation),
- σ_{an} and σ_{ap} : stresses corresponding to A nucleation and propagation (reverse localised transformation).

Those stresses are assumed to linearly depend on the temperature exhibiting the same slope K_T than $\sigma_s(T)$ and $\sigma_f(T)$ transitions previously defined. The diagram given in Fig. 7 is completed respecting:

$$\begin{cases} \sigma_{ms} < \sigma_{mp} < \sigma_{mn} < \sigma_{mf} \\ \sigma_{as} < \sigma_{mf} \\ \sigma_{af} < \sigma_{ms} \\ \sigma_{af} < \sigma_{an} < \sigma_{ap} < \sigma_{as} \end{cases} \tag{29}$$

leading to reverse diagram plotted in Fig. 25. The associated temperature transitions are reported in Table 4.

The direction of the transformation is given by the change of the reduced stress σ_R:

$$\sigma_R = \sigma - K_T T \tag{30}$$

when σ_R is increasing, we use the martensitic boundaries (σ_{mX}) to calculate the driving force. The austenitic boundaries (σ_{aX}) are used otherwise. Fig. 26 sums up the different cases.

Furthermore, the nucleation laws are weakened: a martensite nucleation has to disappear while unloading, whilst an austenite nucleation has to disappear while loading. The loading way is explained by the change of f. Hence, complete Eqs. (15) for forward and reverse transformations are:

$$N_M(x,t) = [\sigma(t) > \sigma_{nm}(x,t)] \wedge [f(x,t-dt) > f(x,t-2.dt)] \tag{31a}$$

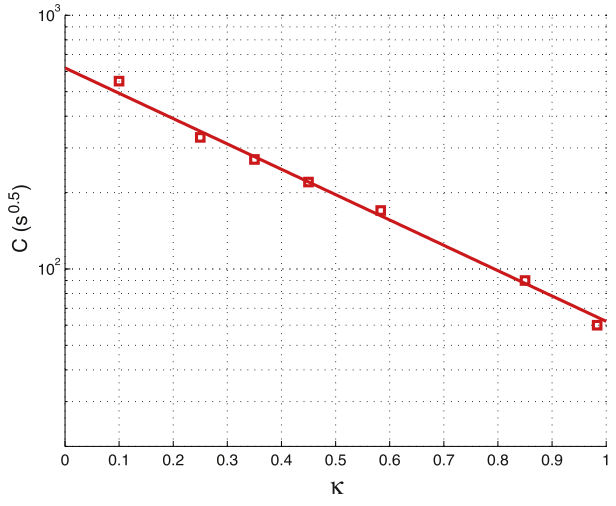

Fig. 24. Variation of C values as function of κ.

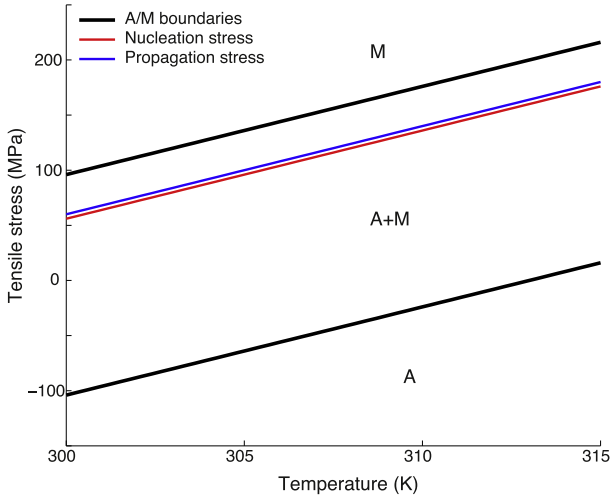

Fig. 25. Homogeneous and localisation boundaries for the reverse transformation: from M to A phases.

Table 4
Material parameters: temperature of homogeneous and localisation boundaries of Clausius–Clapeyron diagram (Fig. 25).

Austenite start	Austenite finish	Nucleation temp.	Propagation temp.
A_s	A_f	A_n	A_p
288	313	293	292.5
K	K	K	K

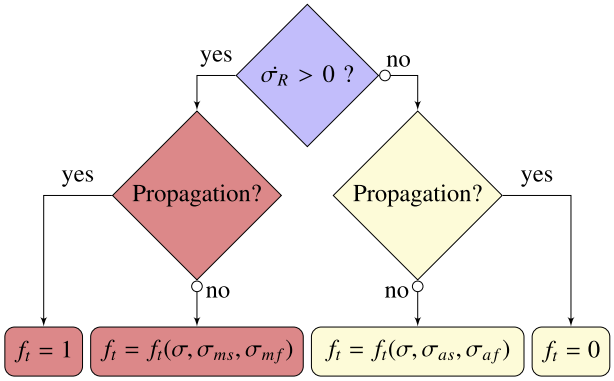

Fig. 26. Calculation of the driving force depending on *M* transformation (direct), and or *A* transformation (reverse).

$$P_M(x,t) = P'_M(x,t) \wedge [f(x,t-dt) > f(x,t-2.dt)] \quad (31b)$$

$$N_A(x,t) = [\sigma(t) < \sigma_{na}(x,t)] \wedge [f(x,t-dt) < f(x,t-2.dt)] \quad (31c)$$

$$P_A(x,t) = P'_A(x,t) \wedge [f(x,t-dt) < f(x,t-2.dt)] \quad (31d)$$

With:

$$P'_M = (N_M(x \pm dx, t) \vee P_M(x \pm dx, t-dt)) \wedge [\sigma(t) > \sigma_{pm}(x,t)] \quad (32a)$$

$$P'_A = (N_A(x \pm dx, t) \vee P_A(x \pm dx, t-dt)) \wedge [\sigma(t) < \sigma_{pa}(x,t)] \quad (32b)$$

N_M, N_A, P_M and P_A being respectively the martensite nucleation, the austenite nucleation, the martensite propagation and the austenite propagation.

6.2. Load-Unload simulation and comparison to experiments

Experimental results of load-unload curves for IRIC test strained at $\dot{\delta}/L_0 = 4.2 \times 10^{-4}\ s^{-1}$ are plotted in Fig. 27(a) and associated modelling are plotted in Fig. 27(b). The initial state of the unloading corresponds to the ultimate state of the loading. This test exhibits a so-called pseudo-elastic effect, and modelling is in accordance.

Fig. 27 exhibits the same stages as those observed in Fig. 9(b) complemented by stages corresponding to the reverse transformation (-end): 0- is the pure elastic strain of austenite, is the onset of

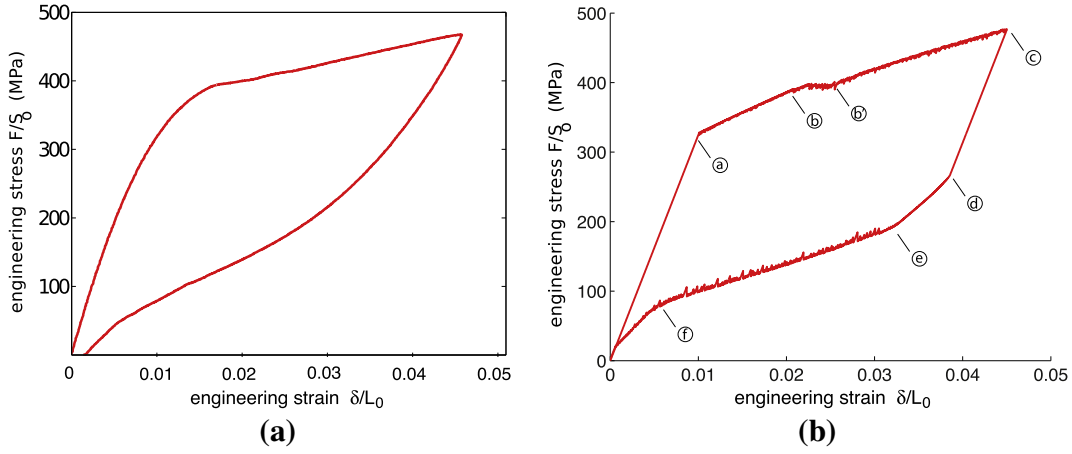

Fig. 27. Experimental (a) *vs.* modelling (b) of load-unload curve at $\dot{\delta}/L_0 = 4.2 \times 10^{-4}\ s^{-1}$.

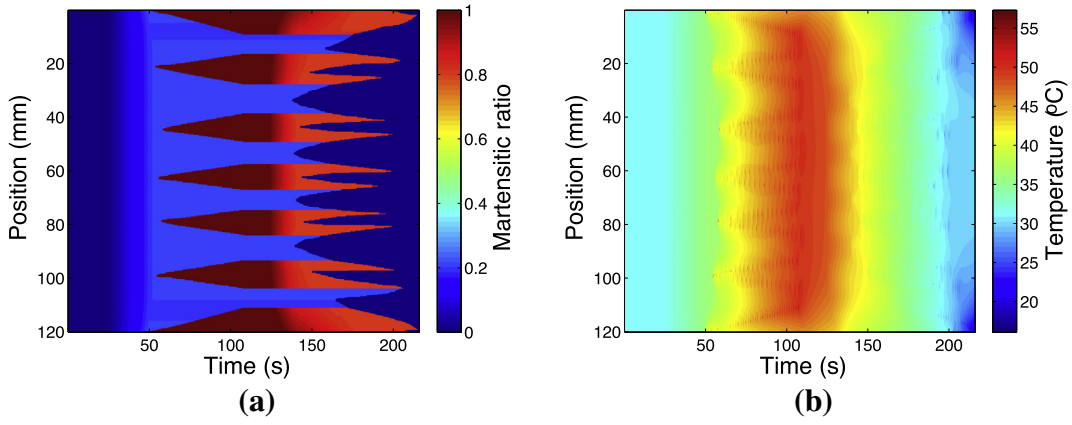

Fig. 28. Modelling of martensite ratio (a) and temperature during the load-unload test at $\dot{\delta}/L_0 = 4.2 \times 10^{-4}\ s^{-1}$.

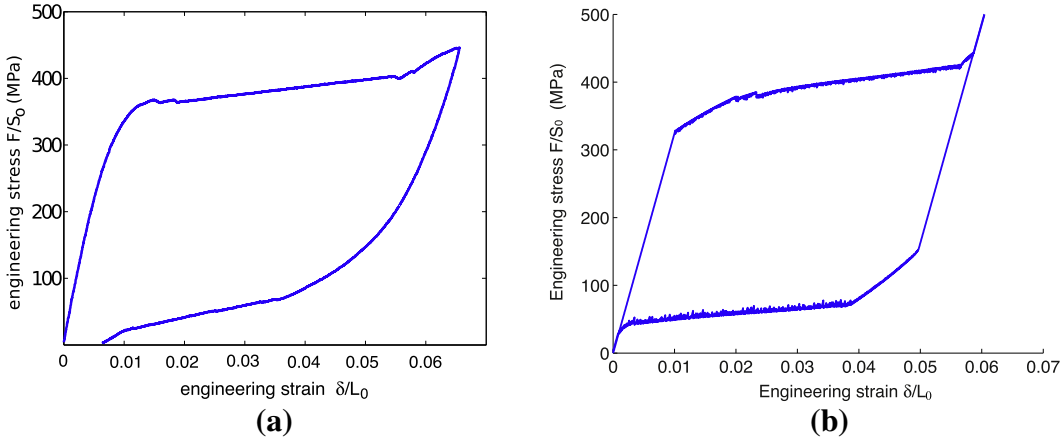

Fig. 29. Experimental (a) *vs.* modelling (b) of load-unload curve at $\dot{\delta}/L_0 = 8.3 \times 10^{-5}\ s^{-1}$.

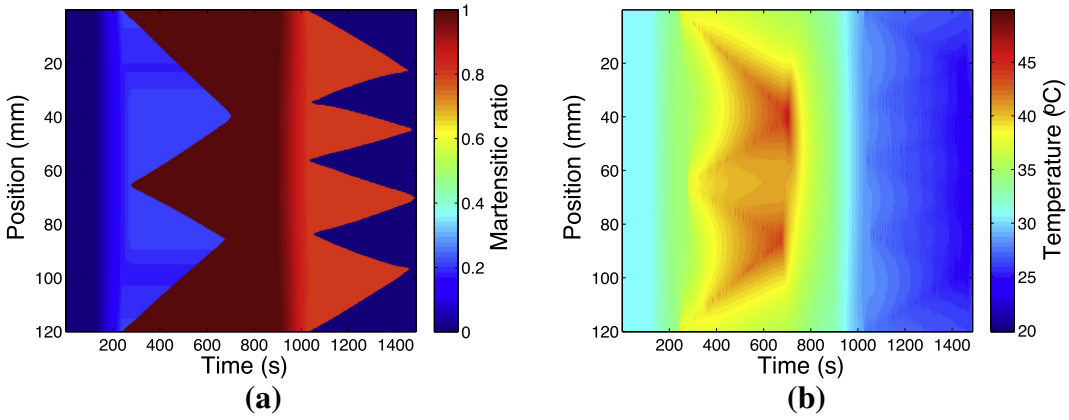

Fig. 30. Modelling of martensite ratio (a) and temperature during the load-unload test at $\dot{\delta}/L_0 = 8.3 \times 10^{-5}\ s^{-1}$.

martensitic transformation. The first nucleation occurs in at the clamps. ' corresponds to a second occurrence. '- is the propagation of all the localisation bands. - is the pure elastic strain of martensite whereas is the on-set of reverse transformation. Hence, -ⓔ is the homogeneous reverse transformation. ⓔ -ⓕ is the propagation of all the inverse transformation bands. The simulation stops after the complete loading/unloading ($u = 0$). The stage corresponding to elastic strain of austenite is reached close to 0 displacement. Fig. 28 shows the result of the corresponding evolution of martensite ratio and temperature.

Fig. 29 allows to compare experimental results of load-unload curves for IRIC test strained at $\dot{\delta}/L_0 = 8.3 \times 10^{-5}\ s^{-1}$. The same stages which were observed in previous results are observed again here. Associated spatiotemporal maps of martensite ratio and temperature are in accordance too.

For all simulations, the stress–strain curves are not symmetric because the thermal state at the beginning of loading, and at the beginning of unloading are not the same. Furthermore, there exists a significative difference between A_s and M_f limits in the Clapeyron diagram. On the other hand the unloading stage starts under a thermal gradient that explains the nucleation of a multi band system during the reverse transformation. (Fig. 30).

At this step, it must be highlighted that the modelling proposed here is not usable in compression in its present form because the Clausius–Clapeyron diagram is not defined in the half plane corresponding to negative stress. Extension to compression requires to define a new set of $\sigma(T)$ limits that do not correspond to a mirror of limits plotted in the positive stress half plane, and that should consequently be identified. The following points must be addressed:

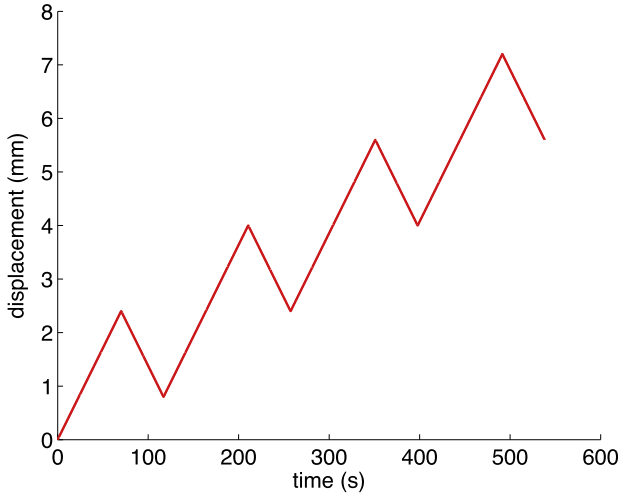

Fig. 31. Incremental loading at a constant absolute strain rate $\dot{\delta}/L_0 = 4.2 \times 10^{-4}\ s^{-1}$.

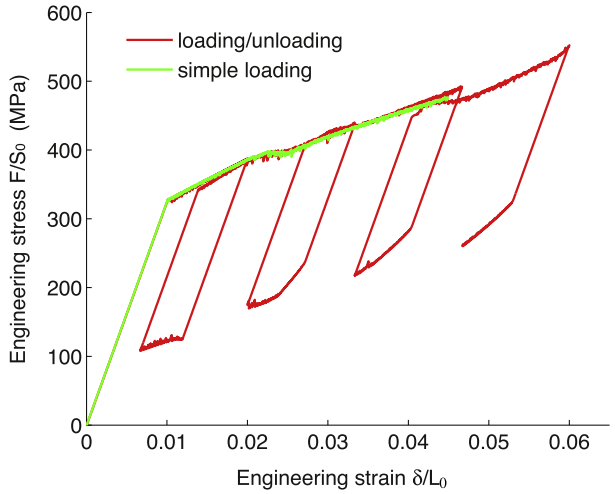

Fig. 32. Modeled stress–strain curve obtained for incremental loading at $\dot{\epsilon} = 4.2 \times 10^{-4}\ s^{-1}$.

- Due to a different selection of variants with positive or negative stress (higher number in compression but lower deformation Maynadier et al., 2011), higher stress levels must be reached in compression to initiate the phase transformation.
- The stress transition cannot be determined *a priori* since the temperature conditions are not known (thermal gradient at the reverse point). A strong decrease in temperature would lead to a martensitic transformation at lower stress level.
- As a consequence the model should not be employed under compression until the implementation of adequate transformation boundaries in the modelling.

The intrinsic test for differentiating forward/reverse transformation allows now to simulate various loading *vs.* time schemes. For instance an incremental loading, as described in Fig. 31 has been simulated keeping the same average strain rate ($\dot{\delta}/L_0 = 4.2 \times 10^{-4}\ s^{-1}$). The associated stress–strain curve is given in Fig. 32 compared to the previous loading–unloading curve. Fig. 33 illustrates the simulated martensite ratio and temperature profiles as a function of time.

At this step, it must be recalled that this one-dimensional model uses a set of parameters partly provided by literature. A proper identification of these parameters could allow more accurate simulation results, especially nucleation/propagation boundaries, which are determinant in the generation of bands. Nevertheless, experimental results and simulations exhibit a qualitative good agreement, which allows us to validate the approach. Furthermore all phenomena that we aimed to model are taken into account: homogeneous transformation, localisation and influence of the strain rate on the number of bands.

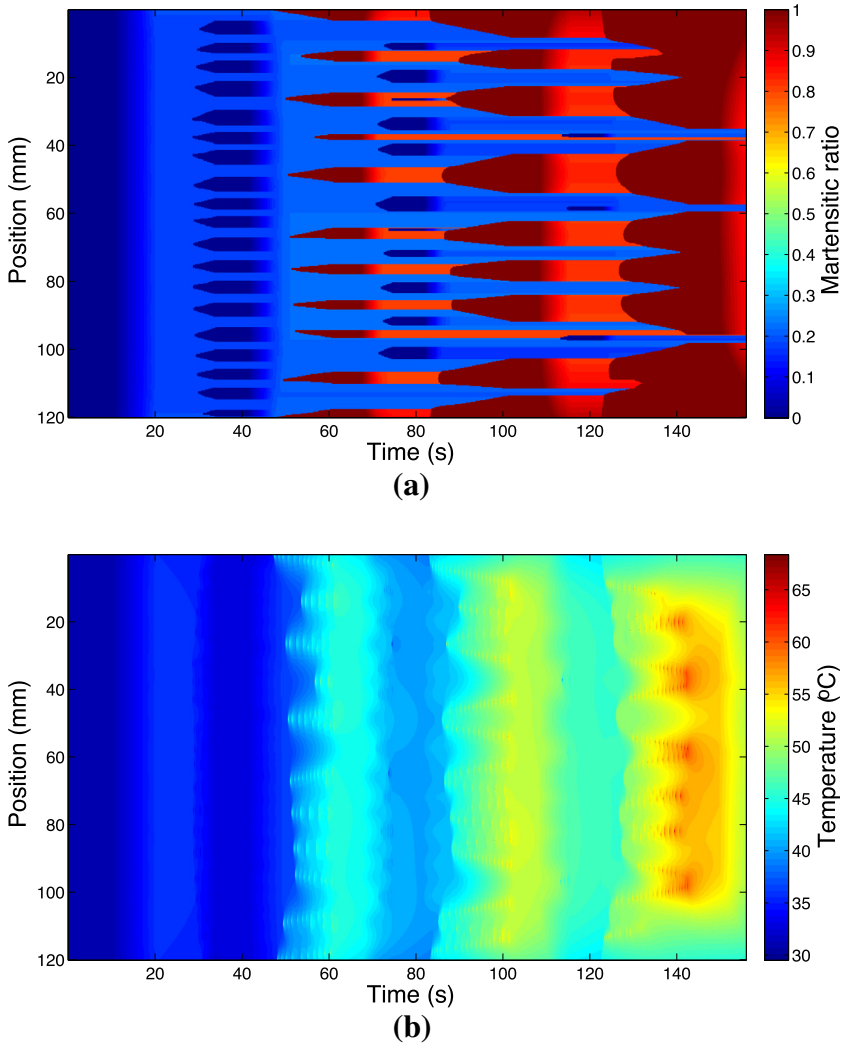

Fig. 33. Spatio-temporal maps of martensite ratio and temperature obtained during incremental loading simulation at $\dot{\epsilon} = 4.2 \times 10^{-4}\ s^{-1}$.

7. Conclusion

The model presented in this paper aims at modelling the pseudo-elastic behaviour of a NiTi-based SMA sample submitted to displacement-controlled uniaxial tensile loading. Focusing on the Clausius–Clapeyron diagram and the domain of existence of each phase, it takes into account the thermal exchanges and the martensitic phase transformation that induces coupled strain and heat generation. Comparisons between simulations carried out at different macroscopic strain rates and some corresponding experiments indicate that the three following key points of the behaviour are suitably described:

- homogeneous strain and transformation,
- localisation of strain and heat emission into localisation bands that enlarge until complete transformation,
- power law dependence of the number of bands to the strain rate,
- transition between convection controlled to conduction controlled nucleation rate of bands for high convection situations.

Moreover, this model handles either forward ($A \rightarrow M$) and reverse ($M \rightarrow A$) transformation, being consequently able to simulate the effect of monotonic or cyclic loading/unloading.

All simulations have been implemented with a set of parameters partly from existing literature, partly from DSC measurement and partly from a previous tensile test where infrared images correlation (IRIC) have been used. Of course, the adequacy of the simulation to the experiments would be greatly improved by the identification of the true thermomechanical constants of (A) and (M) phases (thermal conductivity, specific heat) as well as the slope of $\sigma(T)$ transitions in the Clausius–Clapeyron diagram. The convection conditions adjusted thanks to an IRIC experiment using an inverse method could be more precisely identified using an adequate experimental procedure.

The model has been implemented in Matlab in order to make it versatile enough to allow some optimisations and inverse identification of the thermal conditions for instance. An implementation in a FEM solver is foreseen in the future to reduce the time calculation and to extend this model to 2D or 3D problems. Such extension is required, for example, to give account of the angle of transformation bands vs. the stress axis and stress concentration at the band's fronts. Another work in progress is the introduction of a more physical constitutive law for martensite volume fraction prediction (Maynadier et al., 2011) which takes the R-phase into account.

References

Auricchio, F., Taylor, R.L., Lubliner, J., 1997. Shape-memory alloys: macromodelling and numerical simulations of the superelastic behavior. Comput. Methods Appl. Mech. Eng. 146, 281–312.

Bhattacharya, K., 2003. Microstructure of martensite, materials modelling, Oxford materials, 2007 edition. Oxford University Press.

Chang, B.C., Shaw, J.A., Iadicola, M.A., 2006. Thermodynamics of shape memory alloy wire: modeling, experiments, and application. Continuum Mech. Thermodyn. 18, 83–118.

Chevalier, V., Arbab-Chirani, R., Arbab-Chirani, S., Calloch, S., 2010. An improved model of 3-dimensional finite element analysis of mechanical behavior of endodontic instruments. Oral Surgery, Oral Med. Oral Pathol. Oral Radiol. Endodontology 109, e111–e121.

Christ, D., Reese, S., 2009. A finite element model for shape memory alloys considering thermomechanical couplings at large strains. Int. J. Solids Struct. 46, 3694–3709.

Chrysochoos, A., 2002. La thermographie infrarouge, un outil en puissance pour étudier le comportement des matériaux. Mécanique et Industries 3, 3–14.

De la Flor, S., Urbina, C., Ferrando, F., 2006. Constitutive model of shape memory alloys: theoretical formulation and experimental validation. Mater. Sci. Eng.: A 427, 112–122.

Delpueyo, D., Grédiac, M., Balandraud, X., Badulescu, C., 2012. Investigation of martensitic microstructures in a monocrystalline cu-al-be shape memory alloy with the grid method and infrared thermography. Mech. Mater. 45, 34–51.

Favier, D., Louche, H., Schlosser, P., Orgéas, L., Vacher, P., Debove, L., 2007. Homogeneous and heterogeneous deformation mechanisms in an austenitic polycrystalline Ti-50.8 at.% Ni thin tube under tension. Investigation via temperature and strain fields measurements. Acta Mater. 55, 5310–5322.

Feng, P., Sun, Q., 2006. Experimental investigation on macroscopic domain formation and evolution in polycrystalline NiTi microtubing under mechanical force. J. Mech. Phys. Solids 54, 1568–1603.

He, Y., Sun, Q., 2010. Rate-dependent domain spacing in a stretched NiTi strip. Int. J. Solids Struct. 47, 2775–2783.

Hu, Z., Sun, Q., Zhong, Z., 2006. Numerical simulation for stress-induced phase transformation of SMAs tube under tension. In: Ohno, N., Uehara, T. (Eds.), Eigth Asia-Pacific Symposium on Engineering Plasticity and Its Applications, vol. 340–341, pp. 1181–1186.

Koistinen, D., Marburger, R., 1959. A general equation prescribing the extent of the austenite-martensite transformation in pure iron-carbon alloys and plain carbon steels. Acta Metall. 7, 59–60.

Lagoudas, D.C., Entchev, P.B., Popov, P., Patoor, E., Brinson, L.C., Gao, X., 2006. Shape memory alloys, Part ii: Modeling of polycrystals. Mech. Mater. 38, 430–462.

Levitas, V.I., Stein, E., 1997. Simple micromechanical model of thermoelastic martensitic transformations. Mech. Res. Commun. 24, 309–318.

Maynadier, A., Depriester, D., Lavernhe-Taillard, K., Hubert, O., 2011. Thermo-mechanical description of phase transformation in ni-ti shape memory alloy. Procedia Eng. 10, 2208–2213.

Maynadier, A., Poncelet, M., Lavernhe-Taillard, K., Roux, S., 2012. One-shot measurement of thermal and kinematic fields: infrared image correlation (iric). Exp. Mech. 52, 241–255.

Nemat-Nasser, S., Choi, J.Y., Guo, W.G., Isaacs, J.B., 2005. Very high strain-rate response of a NiTi shape-memory alloy. Mech. Mater. 37, 287–298, New Directions in Mechanics and Selected Articles in Micromechanics of Materials.

Patoor, E., Lagoudas, D.C., Entchev, P.B., Brinson, L.C., Gao, X., 2006. Shape memory alloys, Part i: General properties and modeling of single crystals. Mech. Mater. 38, 391–429.

Pieczyska, E., Gadaj, S., Nowacki, W., Tobushi, H., 2006. Phase-transformation fronts evolution for stress- and strain- controlled tension tests in NiTi shape memory alloy. Exp. Mech. 46, 531–542.

Rappaz, M., Bellet, M., Deville, M., 2003. Modeling in Materials Science and Engineering. Springer Verlag.

Schlosser, P., Louche, H., Favier, D., Orgéas, L., 2007. Image processing to estimate the heat sources related to phase transformation during tensile test of NiTi tubes. Strain 43, 260–271.

Shaw, J.A., 2000. Simulations of localized thermo-mechanical behavior in a NiTi shape memory alloy. Int. J. Plast. 16, 541–562.

Shaw, J.A., 2002. A thermomechanical model for a 1-d shape memory alloy wire with propagating instabilities. Int. J. Solids Struct. 39, 1275–1305.

Shaw, J.A., Kyriakides, S., 1995. Thermomechanical aspects of NiTi. J. Mech. Phys. Solids 43, 1243–1281.

Shaw, J.A., Kyriakides, S., 1997. On the nucleation and propagation of phase transformation fronts in a NiTi alloy. Acta Mater. 45, 683–700.

Thamburaja, P., Nikabdullah, N., 2009. A macroscopic constitutive model for shape-memory alloys: theory and finite-element simulations. Comput. Methods Appl. Mech. Eng. 198, 1074–1086.

Zhang, X., Feng, P., He, Y., Yu, T., Sun, Q., 2010. Experimental study on rate dependence of macroscopic domain and stress hysteresis in NiTi shape memory alloy strips. Int. J. Mech. Sci. 52, 1660–1670.